AMERICAN UNIVERSITY OF BEIRUT

DEVELOPMENT OF GENERAL CIRCULATION MODEL FOR A LAND PLANET IN PARALLEL WITH WEATHER FORECAST AUTOMATION

by

MOHAMMAD HASSAN ALLOUCHE

A thesis
submitted in partial fulfillment of the requirements
for the degree of Master of Engineering
to the Department of Mechanical Engineering
of the Faculty of Engineering and Architecture
at the American University of Beirut

Beirut, Lebanon
December 2014

AMERICAN UNIVERSITY OF BEIRUT

DEVELOPMENT OF GENERAL CIRCULATION MODEL FOR A LAND PLANET IN PARALLEL WITH WEATHER FORECAST AUTOMATION

by

MOHAMMAD HASSAN ALLOUCHE

Approved by:

Issam Lakkis, Associate Professor
Mechanical Engineering — Advisor

Alan Shihadeh, Professor
Mechanical Engineering — Committee Member

Fadl Moukalled, Professor
Mechanical Engineering — Committee Member

Date of thesis defense: 22/12/2014

AMERICAN UNIVERSITY OF BEIRUT

THESIS, DISSERTATION, PROJECT RELEASE FORM

Student Name: ALLOUCHE (Last) MOHAMMAD (First) HASSAN (Middle)

☑ Master's Thesis ○ Master's Project ○ Doctoral Dissertation

☑ I authorize the American University of Beirut to: (a) reproduce hard or electronic copies of my thesis, dissertation, or project; (b) include such copies in the archives and digital repositories of the University; and (c) make freely available such copies to third parties for research or educational purposes.

☐ I authorize the American University of Beirut, **three years after the date of submitting my thesis, dissertation, or project,** to: (a) reproduce hard or electronic copies of it; (b) include such copies in the archives and digital repositories of the University; and (c) make freely available such copies to third parties for research or educational purposes.

Signature

16-01-2015

Date

This form is signed when submitting the thesis, dissertation, or project to the University Libraries

ACKNOWLEDGEMENTS

I would like to thank my supervisor, Professor Issam Lakkis, for the advise and guidance he provided throughout my time as a graduate student. I was lucky to have an advisor who cared for my work, and who was always there for support. I would like to thank Prof Fadl Moukalled, who provided me with enough support and information in the numerical computational field to make the first chapter of the project possible. I would also like to thank Prof Alan Shihadeh and Prof Makram Suidan (Dean of FEA) who gave me the opportunity to have an internship in atmospheric studies at the University of Canterbury, New Zealand where I acquired skills in dealing with numerical weather prediction tools i.e. ARPS and TAPM. Here, I would like to express my gratitude to Dr. Marwan Katurji who helped me grasp the fundamentals of the latter models in a record time.

I would like to express thanks to my family, who were always there to support me no matter how difficult things got. They were always prepared to give me morale and comfort me during the long night of work and research. Completing this work would not have been possible without the support of my peers and friends.

Finally, I would like to thank the American University of Beirut, and the Dean of the FEA without whom the project would not have been complete.

The simulations/predictions (or other items as appropriate) were made using the Advanced Regional Prediction (ARPS) developed by the Center for Analysis and Prediction of Storms (CAPS), University of Oklahoma. CAPS is supported by the National Science Foundation and the Federal Aviation Administration through combined grant ATM92-20009.

AN ABSTRACT OF THE THESIS OF

Mohammad Hassan Allouche for Master of Engineering
Major: Mechanical Engineering

Title: Development of General Circulation Model for a Land Planet In Parallel With Weather Forecast Automation

Large scale circulations of the atmosphere and ocean are not merely driven by chaotic movement of natural fluids, but there are organizing fluid mechanical principles that shape such circulations and drive *Climate Dynamics* in such an ordered fashion. Understanding the physical origins for such **Geostrophic Balanced Flows** patterns in the atmosphere is a key factor to come up with a simplified General Circulation Model that incorporates Radiative Conductive Transfer Balance on **Land Surfaces**.

In parallel with the Climate Model development, setting up a weather forecasting tool for Lebanon hosted by the *Mechanical Engineering Department* at the **American University of Beirut** was the other objective to achieve. The latter involves studying and assessing how well Numerical Weather Prediction Tools (**NWP**) i.e -*Advanced Regional Prediction System* (**ARPS**)- can forecast weather for real case scenarios in Lebanon. Sensitivity study and validation analysis is attained to guarantee a working grid simulation before launching automation.In addition to that, idealized calm situations are simulated to understand thermal circulations modified by the unique geographic terrain under weak synoptic forcings.

CONTENTS

Page

ILLUSTRATIONS

TABLES

CHAPTER I

LAND SURFACE MODEL

A. Introduction

1. Statement of the research question

Large scale circulations of the atmosphere and ocean are not merely driven by chaotic movement of natural fluids, but there are organizing fluid mechanical principles that shape such circulations and drive *Climate Dynamics* in such an ordered fashion [5]. Many physical phenomena drive atmospheric dynamics and climate changes via their interactions which vary on scales from centimeters to the globe, and timescales from seconds to millennia such as: convection, weather systems, the Gulf Stream, and the thermohaline circulation of the ocean; however, radiative transfer theory is a momentous key physics in understanding a major aspect of climate dynamics. The latter involves the transmission of Sun radiation through a leaky greenhouse environment of variable triatomic molecules composition.[1]

The temperature distribution invoked by differential heating results from the competition between the Sun, which tries to warm the tropics more than the poles and thus creating horizontal gradients, and gravity, which tries to remove horizontal contrasts and arrange for warmer fluid to overlie colder fluid. Many physical parameters control and participate in this competition such as[3]:

- The rotation of the Earth.
- The variation of the angle between gravity and rotating axis which is known as β-effect.

[1] Triatomic molecules mainly CO_2 and H_2O - known as greenhouse gases - play a crucial role in the absorption of terrestrial radiation.

- Contrasts between the properties of air and water.

Climate dynamics deal with natural fluids that happen to lie on a rotating planet, and therefore such fluids cannot move in a random manner because they are constrained by Earth rotation. As the horizontal spatial scales timescales lengthen, rotation becomes a significant controlling constraint on the motion of both atmosphere and ocean [5]. Assessment of this effect can be approached using the following dimensionless number "R_o: *Rossby Number*" in Eq. 1, which tells on to how extent would the fluid feel this rotation.

$$R_o = \frac{U \cdot \tau_{rot}}{L} \tag{1}$$

where τ_{rot} is the Earth rotation period, U is the characteristic speed of horizontal currents, and L is the characteristic distance over which the current travels. If R_o is much greater than one, then the timescale of motion $\frac{L}{U}$ is short compared to τ_{rot}, and hence motion won't be influenced by rotation; however, if R_o is much less than one, motion of current will be to a great extent influenced by rotation.

Let us have a rough estimation of R_o for the case of atmosphere which is our case in weather system predictions and meteorology by scaling the parameters involved:

$L \sim 5000$ Km, $U \sim 10\ ms^{-1}$, and $\tau_{rot} = 1$ day $\approx 10^5$ s, which gives $R_{o_{atm}} = 0.2 < 1$. This implies that rotation here is of vital importance. Therefore, it can be deduced that on sufficiently **large** scales, rotation will be a momentous constraint on the fluid motion and consequently in shaping the pattern and structure of air and ocean currents.

Triatomic molecules especially water vapor (H_2O) and carbon dioxide (CO_2) strongly absorb radiation in the same wavelengths that the Earth principally radiates, and this results in warming the Earth surface due to the downward radiation by such particles in the atmosphere which is known as "*Greenhouse Effect*" and eventually adjusting the radiative temperature [5]. On the other side, water vapor distribution is not fixed and it's

driven by motion of air currents which in turn depend on the resulted radiative temperature. Hence, climate forms a closed loop which is illustrated below in figure 1.

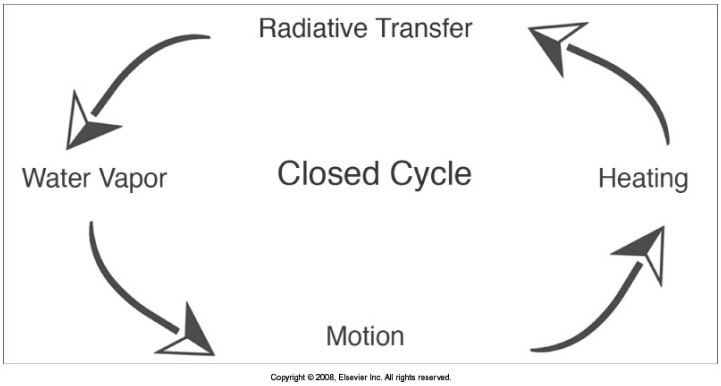

Figure 1: Water vapor interaction with the radiative transfer balance.

2. Objectives of the research statement

Our aim in this research is to build a land surface model (LSM) for Lebanon coupled with the atmosphere to predict geostrophic balanced flows. The prediction of surface temperature characterizes the lower boundary conditions (forcing) to the atmospheric component. Throughout the methodology it will be described how our model is extended to account for major dominant physical processes. As stated earlier, atmospheric circulations are not moving in a disordered manner, but they follow an organized pattern. Integrating the latter with Land surface model as it will be described later will allow us to better predict not only the surface temperature but also atmospheric circulations in terms of wind speed and direction at any elevation.

In our model, we'll imagine everything is reset prior to the existence of any energy source, afterwards Sun is turned on now which invokes differential heating of the earth by radiation. Earth now is conducting heat into the earth (analogous to charging process and this corresponds to a day model), however at night where the Sun is turned off earth starts dissipating heat outwards (analogous to discharging process and this corresponds to a night model). The latter temperature gradient will induce a pressure gradient which will impose atmospheric flows in a designed pattern i.e. flows from high pressure zones to low pressure zones.

B. Literature Review

1. Earth's Energy Budget

Solar Radiation is the major contributor in the "*Earth Energy Budget*", and it affects the Earth's weather processes. Thus, understanding the physics of solar input flux into the "*Earth's System*" is quite important in order to assess this amount of energy intercepted by the surface of the Earth. Many parameters are involved in heating and cooling the surface of the Earth, and such processes are illustrated below in figure 2.

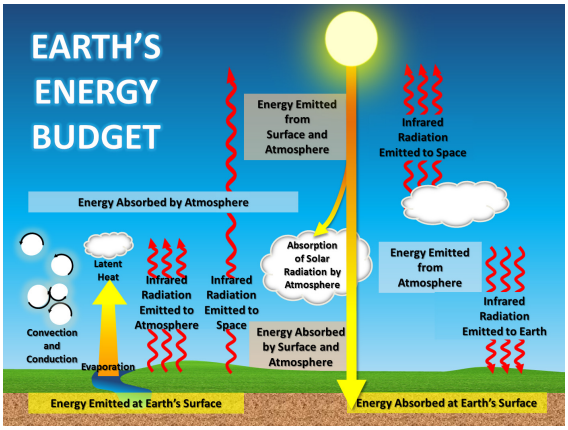

Figure 2: Physical processes involved in surface energy balance.

The Earth receives almost all of its energy from the Sun through penetration of shortwave solar radiation known as "*Insolation*". Part of this energy is trapped within the Earth-Atmosphere System, and the rest leaves in the form of reflected solar radiation or Outgoing long-wave radiation (infrared) [5]. There exists a balance between all forms of energy (Sources and Sinks) which will be introduced gradually in the following modeling sections.Some parts of the Earth such as tropics receive a lot of solar energy imposing a positive heat balance (surplus) while other parts as polar regions receive less solar energy imposing a negative heat balance (deficit) as illustrated in figure 3. The latter phenomenon is known as "*Differential Heating*". This imbalance in radiation absorption provides the basic driving mechanism for the circulation of the atmosphere and, indirectly, the pressure systems which give us our weather [5].

To create some sort of balance, poleward transport of energy surplus is achieved via pressure belts, winds, and ocean currents. Thus the global energy budget is a critical key which affects the amount of energy gain or loss at the Earth's surface level and consequently this has a huge effect on weather and climate dynamics.

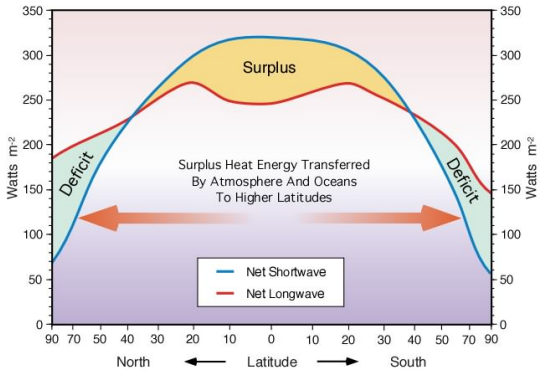

Figure 3: Energy budget variation with latitude.

2. Previous Work "LSM"

a. First Generation: "Manabe bucket model"

It was first described and implemented in a climate model by Manabein (1969) where many assumptions were took to simplify the model [8]:

- No ground heat flux into the earth.
- Spatially constant physical properties of the land.
- No canopy i.e. No vegetation.

The Project for Intercomparison of Landsurface Parameterisation Schemes (PILPS) has shown that the model is inadequate for diurnal to multi-annual scale surface hydrology representation.

b. Second Generation: With Canopy

Vegetation impacts energy and water budgets, momentum transfer. This is the reason why it's accounted for in the second generation where Deardorff found better prediction of ground surface temperature and moisture, with inclusion of a layer of vegetation, and several soil layers were under study [2]. PILPS demonstrated that this new model outperformed the first generation models since it improved modeling of surface atmosphere interactions on the time scale of days:

- Improved precipitation weather forecast (Beljaars et al, 1996)
- Improved European soil temperature prediction (Viterbo et al, 1999).

3. Useful Data

a. Albedo

The Earth's surface has a certain *albedo* α which represents the ratio of reflected $S\uparrow$ to incident solar energy $S\downarrow$ [6] as shown in Eq. 2.

$$\alpha = \frac{S\uparrow}{S\downarrow} \tag{2}$$

The following figure describes the surface albedo distribution on the entire map. Relative discrepancies can be easily distinguished in figure 4.

In Land Surface Models (LSM), the average albedo $\alpha \approx 0.3$.

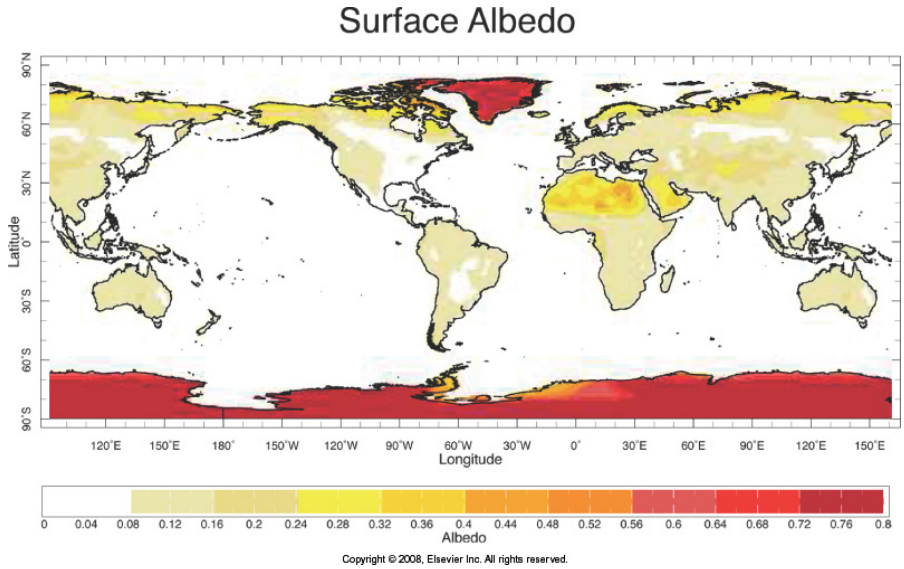

Figure 4: Surface Albedo Worldwide Distribution.

C. Methodology

1. Radiative Transfer Balance Model

a. Earth-Atmosphere Geometry

The Earth is an almost perfect sphere with a mean radius $a = 6370$ km. About 80% of the mass of the atmosphere is contained within the first 10 km altitude due to the influence of gravity. Hence, the atmosphere which envelopes the spherical Earth can be modeled as a thin film of fluid (Air) because its thickness is much smaller compared to the radius of the Earth as depicted in figure 5.

This simplification allows neglecting the curvature of the Earth's surface, thus assuming planar geometry.

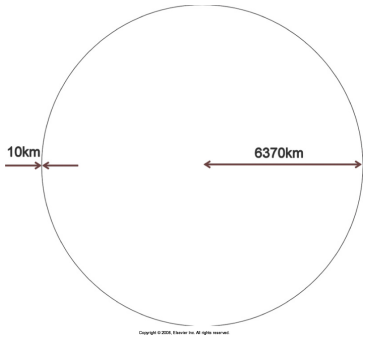

Figure 5: Scaling the atmosphere thickness to the Earth's radius.

b. Leaky Greenhouse Model

The following diagram describes all types of heat radiation exchanges between the Sun "Shortwave radiation major Source", and the Earth-Atmosphere System "Long wave radiation Sources and Sinks".

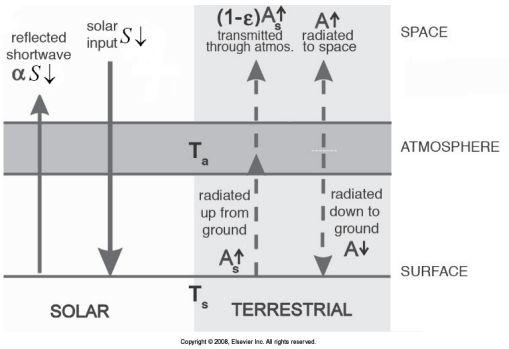

Figure 6: Radiative transfer balance model.

The Stefan-Boltzmann law states the emitted radiation for any surface characterized by a certain surface Temperature $T > 0$ kelvin is proportional to the 4th degree of this surface temperature such that Emitted radiation per unit area $= \sigma T^4$ where $\sigma = 5.67 \times 10^{-8}\ Wm^{-2}K^{-4}$ is the Stefan-Boltzmann constant; however, the latter description works for black bodies where *emissivity* $\varepsilon_{blackbody} = 1$. Real surfaces are characterized by a certain *emissivity* $0 < \varepsilon < 1$ which is quite related to the surface properties (i.e. surface roughness, color...) and it describes on to how extent this surface

acts as a black body (i.e. ε: ratio of the actual emitted flux to the flux that would be emitted by a black body at the same temperature), thus Emitted radiation per unit area for such surfaces $= \varepsilon\sigma T^4$.

The atmosphere as stated earlier is modeled as a thin layer that is completely transparent to Shortwave Solar radiation with a representative temperature T_a, and T_s stands for Earth's surface temperature. This layer has a certain *absorptivity* same as *emissivity*[2] $0 < \varepsilon < 1$ where *absorptivity* represents the fraction absorbed of the upward Long wave -Infrared- terrestrial radiation by the atmosphere[3]. *Absorptivity* ε is quite related to the concentration of triatomic molecules.

The net flux $(1-\alpha)S\downarrow$ into the Earth-Atmosphere system must be in equilibrium on average with the emitted terrestrial radiation $A_s\uparrow = \varepsilon_s\sigma T_s^4$ that is transmitted through atmosphere to Space where ε_s is Earth's surface *emissivity*, and atmospheric radiation $A\uparrow = \varepsilon\sigma T_a^4$ that is radiated to Space which is the same as atmospheric counter radiation $A\downarrow = \varepsilon\sigma T_a^4$ at equilibrium. This can be described by taking the Earth's surface lumped with the atmosphere layer as a control volume, hence the governing heat transfer balance is as follows below in Eq. 3:

$$(1-\alpha)S\downarrow = A\uparrow + (1-\varepsilon)A_s\uparrow \tag{3a}$$

$$(1-\alpha)S\downarrow = \varepsilon\sigma T_a^4 + (1-\varepsilon)\varepsilon_s\sigma T_s^4 \tag{3b}$$

Note that the Earth's surface is an active layer of infinitesimal small thickness where the storage of energy in such a layer is neglected, and it is assumed to neglect conduction in the current model i.e. huge insulation in order to assess the contribution of

[2] Kirchhoff's law states that *absorptivity* equals *emissivity*.

[3]

- If $\varepsilon = 1$, this corresponds to opaque greenhouse model where all terrestrial radiation is trapped within the Earth-Atmosphere System "Overestimated Model".
- If $\varepsilon = 0$, this corresponds to transparent greenhouse model where all terrestrial radiation is transmitted to Space "Underestimated Model".

Shortwave Solar radiation impact on Earth's surface Temperature T_s "*Radiative Equilibrium Temperature*".

The heat transfer balance at the level of the Earth's surface as described above is as follows in Eq. 4:

$$(1-\alpha)S\downarrow + A\downarrow - A_s\uparrow = 0 \tag{4a}$$

$$(1-\alpha)S\downarrow + \varepsilon\sigma T_a^4 - \varepsilon_s\sigma T_s^4 = 0 \tag{4b}$$

Substituting $A\uparrow = A\downarrow = \varepsilon\sigma T_a^4$ from Eq. 3b in Eq. 4b gives T_s "*Earth's Surface Radiative Equilibrium Temperature*" in Eq. 5c:

$$(1-\alpha)S\downarrow + [(1-\alpha)S\downarrow - (1-\varepsilon)\varepsilon_s\sigma T_s^4] - \varepsilon_s\sigma T_s^4 = 0 \tag{5a}$$

$$2(1-\alpha)S\downarrow - \sigma T_s^4((1-\varepsilon)\varepsilon_s + \varepsilon_s) = 0 \tag{5b}$$

$$T_s = \left[\frac{2(1-\alpha)S\downarrow}{\sigma((1-\varepsilon)\varepsilon_s + \varepsilon_s)}\right]^{\frac{1}{4}} = \left[\frac{2(1-\alpha)S\downarrow}{\sigma(2\varepsilon_s - \varepsilon\varepsilon_s)}\right]^{\frac{1}{4}} \tag{5c}$$

To find the relation between T_s "*Earth's Surface Radiative Equilibrium Temperature*" and T_a "*Atmosphere Radiative Equilibrium Temperature*", $(1-\alpha)S\downarrow$ is substituted from Eq. 3b in Eq. 4b. Hence, T_a "*Atmosphere Radiative Equilibrium Temperature*" is related to T_s in Eq. 6b:

$$\left[\varepsilon\sigma T_a^4 + (1-\varepsilon)\varepsilon_s\sigma T_s^4\right] + \varepsilon\sigma T_a^4 - \varepsilon_s\sigma T_s^4 = 0 \tag{6a}$$

$$T_a = \left(\frac{1}{2}\right)^{\frac{1}{4}} T_s \tag{6b}$$

2. Radiative Conductive Transfer Balance Model

a. Earth Heat Flux

The rate at which heat flows through Earth at a depth z below the surface is directly proportional to the temperature gradient as indicated in Eq. 7 where κ is the thermal conductivity $Wm^{-1}K^{-1}$ of the profile material under study (i.e. soil) which describes the ability of the soil to transport thermal energy.

$$G = -\kappa \nabla T = -\kappa \frac{\partial T}{\partial z}\hat{z} \tag{7}$$

Taking a control volume of a certain depth into the Earth as depicted in fig 7 and applying heat transfer balance reveal that changes of G with depth lead to changes of the heat content of the soil in time t as modeled in Eq. 8 where soil heat transfer in planar directions is neglected and accounted for in vertical direction only (z direction). ρ is soil density kgm^{-3}, c is the soil specific heat capacity $Jkg^{-1}K^{-1}$, and $C = \rho c$ is the volumetric heat capacity $Jm^{-3}K^{-1}$

$$\rho c \frac{\partial T}{\partial t} = -\frac{\partial G}{\partial z} \tag{8a}$$

$$\frac{\partial T}{\partial t} = -\frac{1}{C}\frac{\partial G}{\partial z} \tag{8b}$$

Figure 7: Soil control volume of certain depth.

Combining Eq. 7 and Eq. 8b and assuming now for simplicity that κ thermal conductivity doesn't vary with depth lead to the second order partial differential equation (*PDE*) below in Eq. 9, where $\xi = \frac{\kappa}{C}$ is the thermal diffusivity $m^2 s^{-1}$ which describes the

travel velocity of a temperature change in the soil and controls the penetration depth of changes in temperature at surface.

$$\frac{\partial T}{\partial t} = -\frac{1}{C}\frac{\partial}{\partial z}\left(-\kappa\frac{\partial T}{\partial z}\right) = \frac{\kappa}{C}\frac{\partial^2 T}{\partial z^2} \equiv \xi\frac{\partial^2 T}{\partial z^2} \tag{9}$$

b. Updated Surface Energy Balance Model

Extension to the previous model, conduction into the Earth is now considered. In other words, thermal storage inside the Earth is now affected by the felt net radiation $R_n = (1-\alpha)S\downarrow + A\downarrow - A_s\uparrow$ at the surface level. If $R_n > 0$ "*Day Model Case*", then Earth flux[4] is positive $G_{z=0} > 0$ and therefore Earth is storing heat. Also, if $R_n < 0$ "*Night Model Case*", then Earth flux is negative $G_{z=0} < 0$ and therefore Earth is losing heat.

Considering an infinitesimal small thickness of Earth's surface as a control volume allows modeling it as an active layer where thermal storage is neglected. The radiative conductive balance is as follows in Eq. 10:

$$(1-\alpha)S\downarrow + A\downarrow - A_s\uparrow - G_{z=0} = 0 \tag{10a}$$

$$R_n - G_{z=0} = 0 \tag{10b}$$

3. Radiative Conductive Convective Transfer Balance Model

So far, the convective term H is not a player in the model. Now, it will be accounted for where it will show up in the surface energy balance as depicted below in Eq. 11, where T_∞ is the free stream air temperature and h is the convective heat transfer

[4]Fluxes are considered positive when directed toward the surface (Energy Sources) and negative when directed away from the surface (Energy Sinks).

coefficient $Wm^{-2}K^{-1}$.

$$R_n - h(T_s - T_\infty) - G_{z=0} = 0 \tag{11a}$$

$$R_n - H - G_{z=0} = 0 \tag{11b}$$

Characterization of h necessitates knowledge of the external flow of air past the land surface. Therefore, understanding the governing equations for the fluid motion of air is a momentous key to follow up with the very extended model.

4. Equations of Fluid Motion

a. Geostrophic Balance

It's observed that winds and currents happen to flow in a rotating frame of reference (Non-Inertial Frame), thus two apparent non-frequent accelerations will show up in the momentum equation which are: *centrifugal acceleration* $-\Omega \times \Omega \times r$ and *Coriolis acceleration* $-2\Omega \times \mathbf{u}$.

The general governing momentum equation is as follows in Eq.12:

$$\frac{D\mathbf{u}}{Dt} + \frac{1}{\rho}\nabla P + g\hat{\mathbf{z}} = -2\Omega \times \mathbf{u} + -\Omega \times \Omega \times r + F_{fric} \tag{12}$$

Centrifugal acceleration could be expressed as the gradient of a potential as shown below in Eq.13:

$$-\Omega \times \Omega \times r = \nabla\left(\frac{\Omega^2 r^2}{2}\right) \tag{13}$$

Then Eq.12 could be written now in its succinct form in Eq.14 where $\phi = gz - \frac{\Omega^2 r^2}{2}$ is a modified gravitational potential:

$$\frac{D\mathbf{u}}{Dt} + \frac{1}{\rho}\nabla P + \nabla\phi = -2\Omega \times \mathbf{u} + F_{fric} \tag{14}$$

Recall that the thinness of the atmosphere allows us to neglect the Earth's curvature and

to use local Cartesian coordinate system instead. At a certain latitude φ, (x,y,z) coordinates directions point (eastward,northward,upward),so the components of Ω in these coordinates are $(0, \Omega cos\varphi, \Omega sin\varphi)$. Therefore, Coriolis force is expressed in these defined coordinates as follows in Eq.15.

$$\Omega \times \mathbf{u} = (0, \Omega cos\varphi, \Omega sin\varphi) \times (u, v, w) \tag{15a}$$

$$\Omega \times \mathbf{u} = (\Omega cos\varphi\, w - \Omega sin\varphi\, v, \Omega sin\varphi\, u, -\Omega cos\varphi\, u) \tag{15b}$$

Two good approximations could be done in this context. First, it is noted that $\mid u \mid \sim 10 ms^{-1}$ in atmosphere, so $\Omega u \sim 7 \times 10^{-4} ms^{-2}$ which is negligible compared to gravity $\Omega u \ll g$. Second, due to the thinness of the atmosphere and ocean, vertical velocities w are much smaller than horizontal velocities u and v where $w \sim 1 cm\, s^{-1}$. Thus, all components involving w can be neglected, and the Coriolis term is rearranged as follows in Eq.16 where $f = 2\Omega sin\varphi$ and known as the Coriolis parameter.[5] Note that $f \to 0$ at the equator where rotational effects are negligible. Also, $f < 0$ in the southern hemisphere and $f > 0$ in the northern hemisphere.

$$2\Omega \times \mathbf{u} \simeq (-2\Omega sin\varphi\, v, 2\Omega sin\varphi\, u, 0) = f\hat{\mathbf{z}} \times \mathbf{u} \tag{16}$$

Rearranging terms in Eq.14 leads to the following updated form of the momentum equation in Eq.17.

$$\frac{D\mathbf{u}}{Dt} + \frac{1}{\rho}\nabla P + \nabla\phi + f\hat{\mathbf{z}} \times \mathbf{u} = F_{fric} \tag{17}$$

Writing Eq.17 in component form in the Cartesian coordinate system that is defined where hydrostatic approximation is dominant in the z direction leads to the following Eq.18 where F_{fric_x} and F_{fric_y} are the (x,y) components of friction, and the vertical

[5] $\Omega sin\varphi$ is the vertical component of the Earth's rotation rate.

component of friction F_{fric_z} to be negligible compared with gravity.

$$\frac{Du}{Dt} + \frac{1}{\rho}\frac{\partial P}{\partial x} - fv = F_{fric_x} \tag{18a}$$

$$\frac{Dv}{Dt} + \frac{1}{\rho}\frac{\partial P}{\partial y} + fu = F_{fric_y} \tag{18b}$$

$$\frac{1}{\rho}\frac{\partial P}{\partial z} + g = 0 \tag{18c}$$

Eq.18 describes the evolution of atmosphere in a general way. Studying large-scale circulation of the atmosphere i.e. Synoptic scale reduces the general form in Eq.18 where it describes now a subset of possible motions known as *Balanced Flows* that are directly linked to *General Circulation*.

Considering the free atmosphere away from the surface and specifically away from boundary layers where friction is negligible allows us anticipating the free stream air velocity U_∞. Large-scale circulation in the atmosphere as stated previously are characterized by typical magnitude of the horizontal flow component $U \sim 10 ms^{-1}$, characteristic length $L \sim 10^6$ m, and characteristic time $\tau_{rot} = 1$ day $\approx 10^5$ s.

Lagrangian or Material derivative of any fixed identity i.e. $\mathbf{u}$ (horizontal flow component) is as follows in Eq.19:

$$\frac{D\mathbf{u}}{Dt} = \frac{\partial \mathbf{u}}{\partial t} + (\mathbf{u}.\nabla)\mathbf{u} \tag{19}$$

So far, hydrostatic balance dominates in the vertical direction, and friction gets out of the picture in the horizontal. Scaling Eq.18 with the characteristic parameters U, L, and τ_{rot} leads to Eq.20b:

$$\frac{D\mathbf{u}}{Dt} + f\hat{\mathbf{z}} \times \mathbf{u} = \frac{\partial \mathbf{u}}{\partial t} + (\mathbf{u}.\nabla)\mathbf{u} + f\hat{\mathbf{z}} \times \mathbf{u} \tag{20a}$$

$$\frac{\partial \mathbf{u}}{\partial t} + (\mathbf{u}.\nabla)\mathbf{u} + f\hat{\mathbf{z}} \times \mathbf{u} \sim \frac{U}{\tau_{rot}} + \frac{U^2}{L} + fU \tag{20b}$$

The acceleration terms related to the inertia scale as $\frac{U^2}{L}$, and the ratio of the inertia term

to the Coriolis term defines the dimensionless number known as *Rossby Number* as expressed in Eq.21 which could be defined also as a ratio of time scales as expressed in Eq.1.

$$R_o = \frac{U}{fL} \tag{21}$$

Then, near middle latitudes where $\varphi = 45^o, f \simeq \frac{2\Omega}{\sqrt{2}} = 1.03 \times 10^{-4} s^{-1}$, and then $R_{o_{atm}} = \frac{10}{1.03 \times 10^{-4} \times 10^6} \simeq 0.1 < 1$. This implies that Coriolis term dominates the acceleration term, and it turns out that Coriolis forces are balanced by horizontal pressure gradients. This is known as "Geostrophic Balance" as depicted in Eq.22:

$$f\hat{\mathbf{z}} \times \mathbf{u} + \frac{1}{\rho}\nabla P = 0 \tag{22}$$

Eq.22 is only satisfied for small R_o, and it's not applicable at and near the equator. From Eq.22, the geostrophic wind or current can be defined as follows in Eq.23a and in component form as in Eq.23b:

$$\mathbf{u}_g = \frac{1}{f\rho}\hat{\mathbf{z}} \times \nabla P \tag{23a}$$

$$(u_g, v_g) = \left(-\frac{1}{f\rho}\frac{\partial P}{\partial y}, \frac{1}{f\rho}\frac{\partial P}{\partial x} \right) \tag{23b}$$

b. Hydrostatic Balance

As stated in Eq.18c, gravity force is balanced by vertical pressure gradient. This is due to the weakness of friction relative to gravity, and because Large-scale atmospheric circulations are characterized by weak vertical motions[6].

[6]

- $w \sim 1 cm\, s^{-1}$.
- $|\frac{Dw}{Dt}| \ll g$ permits neglecting the acceleration term.

Rearranging Eq.18c as follows in Eq.24:

$$\frac{\partial P}{\partial z} = -\rho g \tag{24}$$

Knowing that air mimics to a big extent ideal gases, thus it obeys the ideal gas law "*Equation of State*" as expressed below in Eq.25:

$$P = \rho RT \tag{25}$$

Plugging density ρ from Eq.25 in Eq.24 leads to Eq.26:

$$\frac{\partial P}{\partial z} = -\frac{P}{RT}\, g \tag{26}$$

It is worth to note now that the atmosphere experiences a non-isothermal profile where the temperature T is not constant but varies linearly with height z[7]. T_s is the surface temperature, and T_a is the atmosphere temperature which were both introduced in the "Radiative Transfer Balance Model" subsection [8]. The trend of temperature variation with height $T(z)$ could be expressed as follows in Eq.27, where $a = \left[\frac{T_a - T_s}{\delta_{thermal}}\right]$ and $b = T_s$ are constants for a specific geographical coordinate (φ,λ).

$$T(z) = \left[\frac{T_a - T_s}{\delta_{thermal}}\right] z + T_s = a\, z + b \tag{27}$$

Integrating Eq.26 from the surface $z = 0$ where $P = P_{atm}$ to a certain height z where $P = P(z)$ is expressed below in Eq.28:

$$\int_{P_{atm}}^{P(z)} \frac{\partial P}{P} = -\int_{z=0}^{z} \frac{g}{RT(z)} \partial z = -\frac{g}{R} \int_{z=0}^{z} \frac{1}{(a\, z + b)} \partial z \tag{28}$$

[7] It's observed that the temperature profile is linear, therefore it sounds physical to assume such a profile.

[8] T_a represents the atmosphere temperature at a certain height $z(T_a) = \delta_{thermal}$ which depicts the thermal boundary layer thickness beyond which T_∞ "free stream air temperature" prevails.

Carrying out the integration in Eq.28 leads to the following expression of $P(z)$ in Eq.29b:

$$ln\left(\frac{P(z)}{P_{atm}}\right) = ln\left(\frac{a\,z+b}{b}\right)^{-\frac{g}{Ra}} \tag{29a}$$

$$\frac{P(z)}{P_{atm}} = \left(\frac{a\,z+b}{b}\right)^{-\frac{g}{Ra}} \Rightarrow P(z) = P_{atm} \times \left(\frac{b}{a\,z+b}\right)^{\frac{g}{Ra}} \tag{29b}$$

The coefficient multiplied by P_{atm} in Eq.29b describes the steepness of *decaying* pressure with elevation which is function of the geographical coordinate (*x-y horizontal plane*). Moreover, this coefficient is highly influenced by the surface temperature forcing T_s.

c. Conservation of Mass "Continuity"

Applying conservation of momentum in the defined local Cartesian coordinate allows deriving the geostrophic wind far away from the surface. We are after predicting the pressure with respect to height $P(z)$ at any node (φ,λ) in the x-y horizontal plane, and this means full knowledge of the *3D field of pressure* $P(x,y,z)$.

The latter step allows prediction of the geostrophic wind u_g, v_g at any node but away from the surface. Therefore, applying conservation of mass in differential form gives Eq.30a, and for an incompressible flow gives Eq.30b which implies it is nondivergent. Hence, knowing the horizontal flow component u_g, v_g allows knowing the third velocity component w_g, and therefore characterizing **3D flow patterns**[9].

$$\frac{D\rho}{Dt} + \rho\nabla.\mathbf{u} = 0 \tag{30a}$$

$$\nabla.\mathbf{u} = \frac{\partial u}{\partial x} + \frac{\partial v}{\partial y} + \frac{\partial w}{\partial z} = 0 \tag{30b}$$

[9] *Outflows* exist when $\frac{\partial w}{\partial z} > 0$, and *Inflows* exist when $\frac{\partial w}{\partial z} < 0$.

5. Numerical Solution to the Model

As derived in Eq. 9, the governing equation for temperature is the transient one-dimensional heat diffusion. Rearrangement of the terms leads to the general scalar equation as presented below in Eq. 31:

$$\rho c \frac{\partial T}{\partial t} = \frac{\partial}{\partial z}\left(\kappa \frac{\partial T}{\partial z}\right) \tag{31}$$

a. Finite Volume Method: Spatial Discretization

Consider a grid point cluster as shown below in fig 8 as control volume (*cv*) of size $(\Delta z)_P$ where P is the grid point representative (*node*) of this control volume, N and S are *nodes* of neighbor control volumes (north and south respectively), n and s represent north and south faces of such a *cv*, and δz is nodal distance (i.e. $(\delta z)_n$ is the distance between node N and node P).

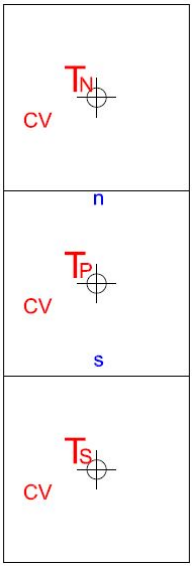

Figure 8: Cluster nodes.

Using "*Gauss' Divergence Theorem*", the volume integral of any scalar quantity Φ over a certain control volume Ω is converted to surface integral over dS where the order of equations is reduced by one as presented below in Eq. 32[10] [7]:

$$\int\int_{\Omega} (\nabla\Phi)\, d\Omega = \oint_{\partial\Omega} \Phi\, dS \tag{32}$$

Handling the diffusion term which is the right hand side term of Eq. 31 for now, and integrating this term over the *cv* lead to the following semi-discretized form in Eq. 33 [7].

$$\int_n^s \frac{\partial}{\partial z}\left(\kappa\frac{\partial T}{\partial z}\right) \Rightarrow \left(\kappa\frac{\partial T}{\partial z}\right)_s - \left(\kappa\frac{\partial T}{\partial z}\right)_n \tag{33}$$

Eq. 33 is a semi-discretized equation for now because some profile must be assumed at the faces to evaluate the gradient terms thus deriving the fully discretized form. It will be assumed that T varies *linearly* across the faces (i.e. between the nodes) as shown in fig , then:

$$\left(\kappa\frac{\partial T}{\partial z}\right)_s = \kappa_s \frac{T_S - T_P}{(\delta z)_s} \tag{34}$$

Now Eq. 33 can be written in the fully discretized form as shown below in Eq. 35

$$\int_n^s \frac{\partial}{\partial z}\left(\kappa\frac{\partial T}{\partial z}\right) \Rightarrow \kappa_s \frac{(T_S - T_P)}{(\delta z)_s} - \kappa_n \frac{(T_P - T_N)}{(\delta z)_n} \tag{35}$$

[10] Closed loop integral $\oint_{\partial\Omega}$ over surface $\partial\Omega$ denotes summation over all the faces constituting the control volume Ω.

b. Finite Volume Method: Temporal Discretization

Handling now the unsteady term which is the left hand side of Eq. 31, and integrating this term over *time* (i.e. certain time step Δt) lead to the following semi-discretized form in Eq. 36 where it is assumed that ρc to be constant.

$$\int_t^{t+\Delta t} \rho c \frac{\partial T}{\partial t}\, dt \Rightarrow \rho c \int_t^{t+\Delta t} \frac{\partial T}{\partial t}\, dt \tag{36}$$

The idea here is to obtain the solution for temperature by marching in *time* knowing an initial temperature distribution since *time* is a one way coordinate [7]. Let T_P^n denotes the old (initial) grid point value of temperature at time t, and T_P^{n+1} denotes the new (unknown) grid point value of temperature to be solved for at time $t = t + \Delta t$ where it is assumed that the grid point value of temperature (T_P) prevails throughout the control volume. Eq. 36 can be written now in the form shown below in Eq. 37:

$$\rho c \int_t^{t+\Delta t} \frac{\partial T}{\partial t}\, dt \Rightarrow \rho c (T_P^{n+1} - T_P^n) \tag{37}$$

c. Explicit, Crank-Nicolson, and Fully Implicit Schemes

Some profile assumption must be made to describe the behavior of the nodal temperature variation over the time interval from t to $t + \Delta t$. The following Eq. 38 assumes some weighing factor f of the future nodal temperature at $t + \Delta t$ where $(f \in [0,1])$[11] [7]:

[11]

- If $f = 0 \rightarrow$ Explicit Scheme.
- If $f = 0.5 \rightarrow$ Crank-Nicolson Scheme.
- If $f = 1 \rightarrow$ Fully Implicit Scheme.

$$\int_t^{t+\Delta t} T_P \, dt = [f T_P^{n+1} + (1-f) T_P^n] \Delta t \tag{38}$$

d. Final Discretization Equations

Integrating Eq. 31 over the control volume (*P grid point cluster*) and over the time interval from t to $t+\Delta t$ could be handled now simultaneously after performing spatial and temporal discretization solely where the order of integrations is chosen according to the nature of the term as described below in Eq. 39 [7].

$$\rho c \int_n^s \int_t^{t+\Delta t} \frac{\partial T}{\partial t} \, dt dz = \int_t^{t+\Delta t} \int_n^s \frac{\partial}{\partial z} \left(\kappa \frac{\partial T}{\partial z} \right) \, dz dt \tag{39a}$$

$$\rho c \Delta z (T_P^{n+1} - T_P^n) = \int_t^{t+\Delta t} \left[\kappa_s \frac{(T_S - T_P)}{(\delta z)_s} - \kappa_n \frac{(T_P - T_N)}{(\delta z)_n} \right] \, dt \tag{39b}$$

Invoke Eq. 38 now:

$$\begin{aligned} \rho c \frac{\Delta z}{\Delta t} (T_P^{n+1} - T_P^n) = & f \left[\kappa_s \frac{(T_S^{n+1} - T_P^{n+1})}{(\delta z)_s} - \kappa_n \frac{(T_P^{n+1} - T_N^{n+1})}{(\delta z)_n} \right] + \cdots \\ & (1-f) \left[\kappa_s \frac{(T_S^n - T_P^n)}{(\delta z)_s} - \kappa_n \frac{(T_P^n - T_N^n)}{(\delta z)_n} \right] \end{aligned} \tag{39c}$$

Rearranging terms in the following form:

$$\begin{aligned} \left(\rho c \frac{\Delta z}{\Delta t} + \frac{f \kappa_s}{(\delta z)_s} + \frac{f \kappa_n}{(\delta z)_n} \right) T_P^{n+1} = & \left(\frac{f \kappa_s}{(\delta z)_s} \right) T_S^{n+1} + \left(\frac{f \kappa_n}{(\delta z)_n} \right) T_N^{n+1} + \cdots \\ & \left(\rho c \frac{\Delta z}{\Delta t} - (1-f) \frac{\kappa_s}{(\delta z)_s} - (1-f) \frac{\kappa_n}{(\delta z)_n} \right) T_P^n + \cdots \\ & \left((1-f) \frac{\kappa_s}{(\delta z)_s} \right) T_S^n + \left((1-f) \frac{\kappa_n}{(\delta z)_n} \right) T_N^n \end{aligned} \tag{39d}$$

To simplify things, the following coefficients are defined:

1. $a_S = \frac{\kappa_s}{(\delta z)_s}$
2. $a_N = \frac{\kappa_n}{(\delta z)_n}$
3. $a_P^o = \rho c \frac{\Delta z}{\Delta t}$
4. $a_P = a_P^o + f a_S + f a_S$

Eq. 39d can be written now in terms of the above listed coefficients in the generalized discretized from as shown below in Eq. 40b, where the central gird point T_P appears on the left hand side of the equation, while the neighbor nodes (T_S and T_N) and the constant term b appear on the right hand side of the equation.

$$\begin{aligned} a_P T_P^{n+1} = {} & f a_S T_S^{n+1} + f a_N T_N^{n+1} + \cdots \\ & \left(a_P^o - (1-f)a_S - (1-f)a_N\right) T_P^n + \cdots \\ & \left((1-f)a_S\right) T_S^n + \left((1-f)a_N\right) T_N^n \end{aligned} \tag{40a}$$

Let $b = \left(a_P^o - (1-f)a_S - (1-f)a_N\right) T_P^n + \left((1-f)a_S\right) T_S^n + \left((1-f)a_N\right) T_N^n$, then:

$$a_P T_P^{n+1} = f a_S T_S^{n+1} + f a_N T_N^{n+1} + b \tag{40b}$$

The future value of the nodal temperature T_P^{n+1} appears on the left hand side of Eq. 40b while the future value of the neighbor nodal temperatures (T_S^{n+1} and T_N^{n+1}) and the constant term b appear on the right hand side of Eq. 40b, This can be generalized in the following discretized standard form in Eq. 41:

$$a_P T_P^{n+1} = \sum a_{nb} T_{nb}^{n+1} + b \tag{41}$$

e. Initial and Boundary Conditions

The initial condition of temperature at the surface level $T^n_{z=0} = T_s$ is calculated using Eq. 5c in the "*Radiative Transfer Balance Model*" section. The calculated temperature is assumed to be uniform along the whole computational depth $z = \ell$. Therefore, marching in time is done relative to this assumed profile of initial condition.

The lower boundary condition is taken as *"Dirichlet Boundary Condition"* as expressed in Eq. 42 due to the fact that temperature at a certain depth from the surface remains constant during the period considered such as days. This is referred to as the *mean earth temperature*.

$$T_{z=\ell} = T_{specified} \tag{42}$$

The top boundary condition for the **Radiative Conductive Transfer Balance Model** is determined through an iterative computation where it's taken as *"Von Newmann Boundary Condition"* i.e. Flux is specified using Eq. 10b or as expressed below in Eq. 43:

$$G_{z=0} = R_n \tag{43}$$

Recall that the net Radiation R_n is expressed as described below in Eq. 44:

$$R_n = (1-\alpha)S\downarrow + A\downarrow - A_s\uparrow \tag{44a}$$

$$R_n = (1-\alpha)S\downarrow + \varepsilon\sigma T_a^4 - \varepsilon_s\sigma T_s^4 \tag{44b}$$

Taking the Earth's surface lumped with the atmosphere layer as a control volume as modeled previously in the *"Radiative Transfer Balance Model"* but allowing now for conduction into the earth i.e. removing the insulation, hence the governing heat

transfer balance is adjusted to account for conduction as follows below in Eq. 45

$$(1-\alpha)S\downarrow = A\uparrow + (1-\varepsilon)A_s\uparrow + G_{z=0} \tag{45a}$$

$$(1-\alpha)S\downarrow = \varepsilon\sigma T_a^4 + (1-\varepsilon)\varepsilon_s\sigma T_s^4 + G_{z=0} \tag{45b}$$

Rearranging terms of Eq. 45b, it's found that $\varepsilon\sigma T_a^4 = (1-\alpha)S\downarrow - (1-\varepsilon)\varepsilon_s\sigma T_s^4 - G_{z=0}$. Substituting again in Eq. 44b, R_n which is equal to $G_{z=0}$ is updated now as follows in Eq. 46b:

$$R_n = G_{z=0} = (1-\alpha)S\downarrow + ((1-\alpha)S\downarrow - (1-\varepsilon)\varepsilon_s\sigma T_s^4 - G_{z=0}) - \varepsilon_s\sigma T_s^4 \tag{46a}$$

$$R_n = G_{z=0} = (1-\alpha)S\downarrow - \left(\frac{(1-\varepsilon)\varepsilon_s\sigma T_s^4 + \varepsilon_s\sigma T_s^4}{2}\right) \tag{46b}$$

As it can be seen that the top boundary condition is nonlinear and part of the solution itself as described in Eq. 47; therefore as for the initial condition, $T_{z=0}$ which is equal to T_s will be calculated using the *"Radiative Transfer Balance Model"*.

$$G_{z=0} = (1-\alpha)S\downarrow + FUN(\varepsilon,\varepsilon_s)\sigma T_s^4 \tag{47}$$

The top boundary condition for the **Radiative Conductive Convective Transfer Balance Model** is updated now to account for the convective term where it's taken as *"Von Newmann Boundary Condition"* i.e. Flux is specified as expressed below in Eq.48:

$$G_{z=0} = R_n - h(T_s - T_\infty) \tag{48a}$$

$$G_{z=0} = \left[(1-\alpha)S\downarrow + FUN(\varepsilon,\varepsilon_s)\sigma T_s^4\right] - h(T_s - T_\infty) \tag{48b}$$

The calculated T_s is assumed known now and will be plugged in Eq. 46b for the *Radiative Conductive Transfer Balance Model* or in Eq. 48b for the *Radiative*

Conductive Convective Transfer Balance Model, hence the flux is specified. The discretized model can now be solved, and a new nodal distribution of temperature is obtained. The new calculated T_s is now inserted in Eq. 46b for the *Radiative Conductive Transfer Balance Model* or in Eq. 48b for the *Radiative Conductive Convective Transfer Balance Model* to correct the assumed flux and feed it again as an updated boundary condition to resolve the temperature distribution. This process will be repeated iteratively at each **time step** Δt to make sure the relative error between the last flux and the updated one is much less than 10^{-3}.

D. Results

1. Model Parameters

The surface and profile of land under study here is *Impermeable Solid Rock* with no moisture content because it's not accounted for **latent heat** in the surface energy balance and therefore it's not accounted for the change of rock water content in the profile caused evaporation from ground surface if it were to exist [12]. Rock properties are summarized in table 1:

Model Profile	Density $\rho(kgm^{-3})$	Specific Heat $c(Jkg^{-1}K^{-1})$	Thermal Conductivity $\kappa(Wm^{-1}K^{-1})$	Depth $z=\ell(m)$	Albedo α	Emissivity $\varepsilon_s = 1-\alpha$
Rock	2700	750	0.2	15	0.3	0.7

Table 1: Rock Properties.

The model is applied for a random day in the year that is chosen to be October 5th at 12:00 noon[13] for *Beirut City*[14]. The *mean earth temperature* is expressed in Eq.49, and this is a typical observed temperature for the month of *October*. Thus, this summarizes the *"Lower Dirichlet Boundary Condition"*.

[12] Water content highly affects the thermal heat capacity and conductivity of the profile under study if it were to exist.

[13] $N = 277$ (Day Number) and $CT = 12$ (Clock Time).

[14] $\varphi = 33.8^o$ (Latitude) and $\lambda = 35.51^o$ (Longitude).

$$T_{z=\ell=15m} = T_{specified} = 288K \tag{49}$$

Regarding the *"Top Von Newmann Boundary Condition"*, it's stated earlier in Eq.47 and Eq.48b. Note that this boundary condition is changing with time i.e. new boundary condition every time step due to $S\downarrow(t)$. Under-Relaxation factor is applied $(URF = 0.5)$ between the old flux and the new one at **each** time step to avoid divergence. The atmosphere layer is represented by an effective emissivity $\varepsilon = 0.6$ which reflects a certain random concentration of CO_2 and H_2O.

Fully Implicit Scheme is adopted to handle the unsteady term with maximum time step attained $\Delta t = 5sec$. The transience period is one day.

Number of control volumes used is $Nz = 100$ where stretching factor is applied $str_f = 1.2$ near the top and lower boundaries where the whole physics lies.

Some of the Earth-Atmosphere characteristics that are used in the model are summarized below in table 2.

Earth's Rotation Rate $\Omega(s^{-1})$	Earth's Mean Radius $R_{earth}(m)$	Surface Gravity g (ms^{-2})	Atmospheric Pressure P_{atm} (pa)	Critical Height $\delta_{thermal}(m)$	Universal Gas Constant R $(Jmol^{-1}K^{-1})$
7.27×10^{-5}	6.37×10^{6}	9.81	101325	6800	286.9

Table 2: Earth-Atmosphere Characteristics.

2. Model Output

a. Radiative Conductive Transfer Balance Model

The surface temperature T_s profiles with respect to time for the same day (October 5th corresponding to $N = 277$) are superposed on the same plot as shown in figure 9. To cancel out the effect of the assumed initial profile $T(z,t=0)$, the same 1 day-simulation is repeated in a consecutive manner where the initial condition is **only**

changed in every new 1 day-simulation i.e. for the kth simulation $T_k(z,t=0) = T_{k-1}(z,t=1day)$. It could be inferred that when T_s profile starts to repeat a cycle, then the effect of the assumed initial profile is eliminated. It is noticed in figure 9 that after 37 repetitions of the 1 day-simulation, the output profile T_s is invariant which means that the initial condition fed to the 37th 1 day-simulation sounds physical for **Radiative Conductive Transfer Balance Model**.

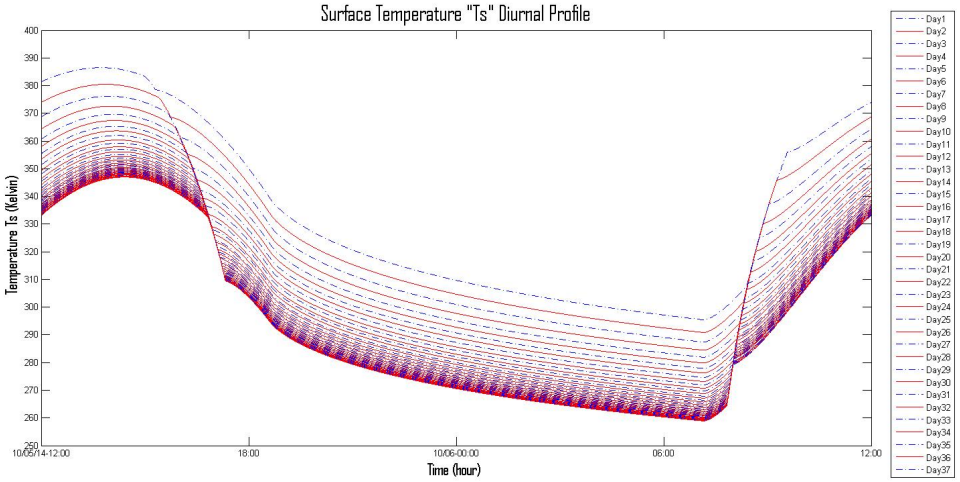

Figure 9: Surface Temperature T_s diurnal profile.

The peak surface temperature $(T_s \approx 340K)$ occurs around 2 : 00 p.m, then the temperature starts decaying afterwards. The minimum temperature reached $(T_s \approx 260K)$ is around 7 : 00 a.m where the felt net radiation R_n starts to shift sign from negative "night" to positive "day". It is realized that the range of temperature variation is quite big which is physical here because the atmosphere is not a participating medium in the current model in terms of convection currents that are responsible for decreasing the surface temperature during the day and increasing the surface temperature during night i.e. narrowing the range of the diurnal temperature variation.

b. Geostrophic Field

The whole earth is discretized in a way that respect the length scales ($L \sim 10^6$) m for Large-scale Balanced flows as shown in figure 10. 10^o latitude resolution and 15^o longitude resolution satisfy the latter condition. One dimensional solving of the surface energy balance is initialized at every node[15]. The previous step provides the diurnal surface temperature forcing around the globe which in turns drives the atmosphere. Time step reached after starting with more physical initial conditions is $\Delta t = 150sec$.

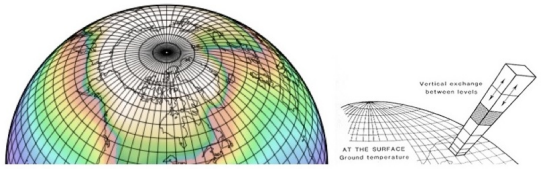

Figure 10: Global discretization.

The shortwave solar radiation intercepted by the globe for October 5th at 12 : 00 p.m in Beirut time is depicted in figure 11.

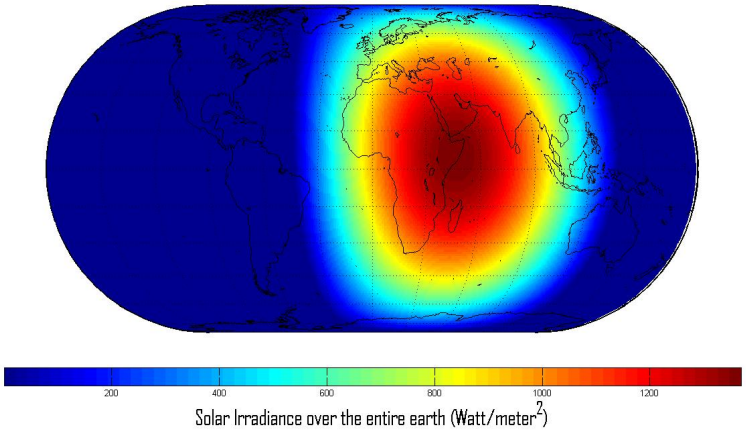

Figure 11: Global shortwave solar radiation with reference to Beirut at noon.

[15]Before launching the solver at every node, the initial conditions for the 37th 1 day-simulation are loaded.

Figure 12 gives an idea about the resultant pressure field at different altitudes caused by differential heating and hydrostatic balance.

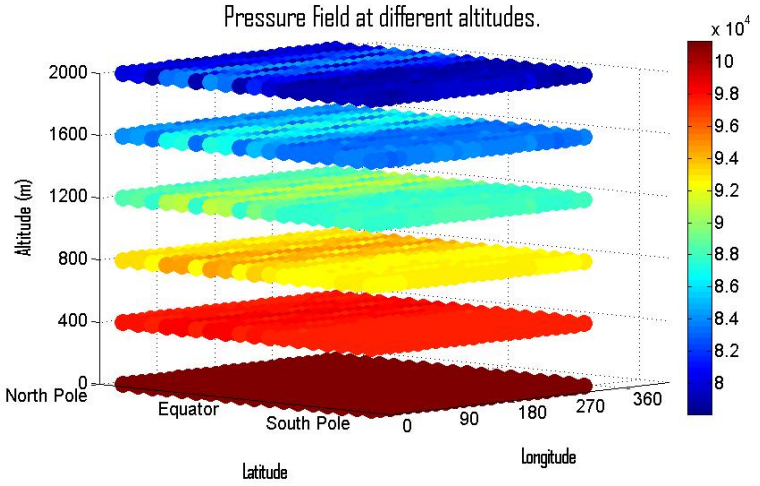

Figure 12: Pressure field at different altitudes in (Pa).

As going away from the surface, the ageostrophic motion shifts to be geostrophic where Coriolis forces are balanced by pressure gradients in the horizontal resulting in a steady flow (zero acceleration). Ideally, under the effect of the pressure-gradient force, the air parcel begins to flow along the gradient from high to low pressure i.e. perpendicularly to the isobars [16], but as the air parcel acquires speed, the increasing Coriolis acceleration causes it to curve to the right (Case of *northern hemisphere*). The geostrophic flow must be parallel to the isobars where the Coriolis force exerted is in the direction directly opposite of the pressure-gradient force. In the *northern hemisphere*, the geostrophic flow is such that the higher pressure is to the right of the flow; air flows clockwise around a center of high pressure and counterclockwise around a center of low pressure as illustrated in figure 13. The direction of flow is reversed in the *southern hemisphere*[17].

Having a closer look at the pressure field obtained in figure 12, it is noticed that horizontal gradients start to develop at high altitudes (away from the surface). This is

[16] Isobars are lines of constant pressure.

[17] A center of high pressure is called an anticyclone or simply a High. A center of low pressure is called a cyclone or simply a Low.

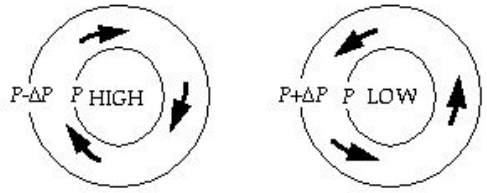

Figure 13: High and Low pressure systems in northern hemisphere.

due to differential heating which invokes temperature contrast between the hot equator and the cold poles. As long as there is no flow of air between any two nodes, this means the total air columns over each node remain the same i.e no pressure gradient. However, the higher temperature over the equator results in a larger atmospheric scale height, so that pressure above equator is greater than the pressure above any offset neighboring node at a certain *altitude* above the surface. This pressure difference causes the air up to flow from the equator to the neighboring node, decreasing the mass of the air column over the equator.

In the below figure 14, geostrophic field is investigated at an elevation of 1200 m at 12 : 00 p.m in Beirut time on the entire globe.

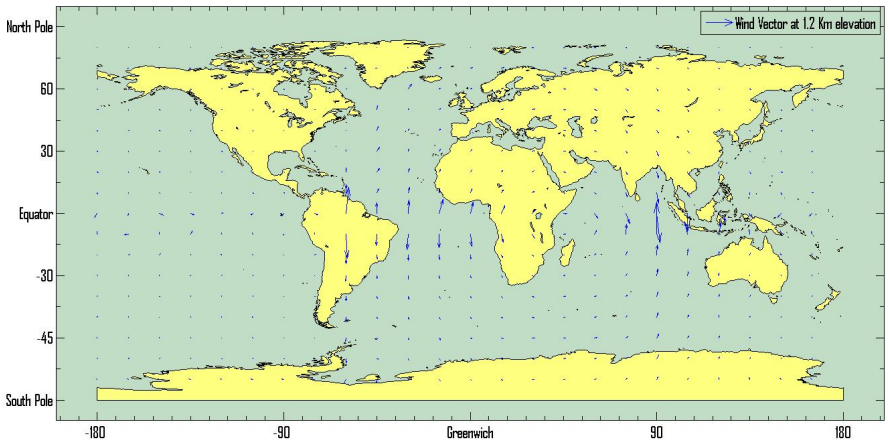

Figure 14: Developed geostrophic field on the entire globe.

Zones that are exposed to solar radiation (Day Model) at this time will experience an anticyclone near the equator at such an altitude, then the general circulation must be clockwise in the *northern hemisphere* around this High center and anticlockwise in the *southern hemisphere* around this High center as illustrated in figure 15. Air in the high-altitude branches of the **Hadley circulation** cells blowing from the equator to the pole is accelerated by the Coriolis force as it moves poleward, eventually breaking down into an unstable flow. Thus it is observed that the **Hadley cells** extend only from the equator to about 30^o latitude. At 30^o the air is pushed down, producing the subtropical high-pressure belts at low-altitude. This is known as "**Subsidence**"

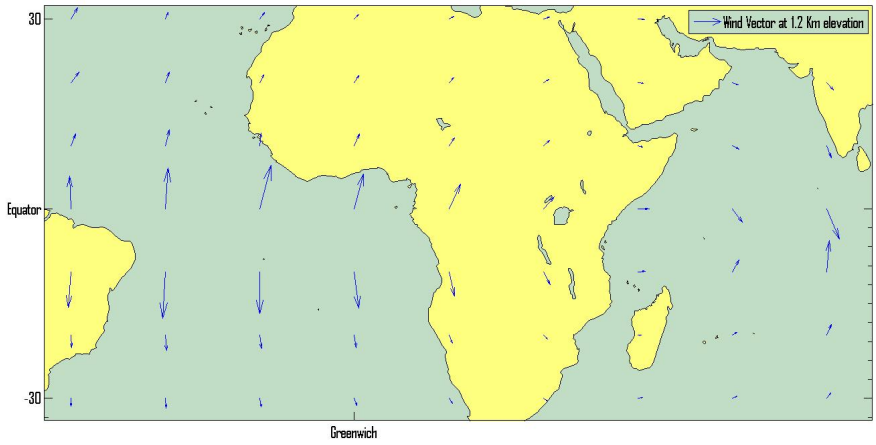

Figure 15: Developed geostrophic field in zones at day times.

On the other hand, zones that are not exposed to solar radiation (Night Model) at this time will experience a cyclone near the equator at such an altitude, then the general circulation must be anticlockwise in the *northern hemisphere* around this Low center and clockwise in the *southern hemisphere* around this Low center as depicted in figure 16.

The magnitude of the resultant wind vector scales to the order of ones ms^{-1} which meets the scales of large scale flows.

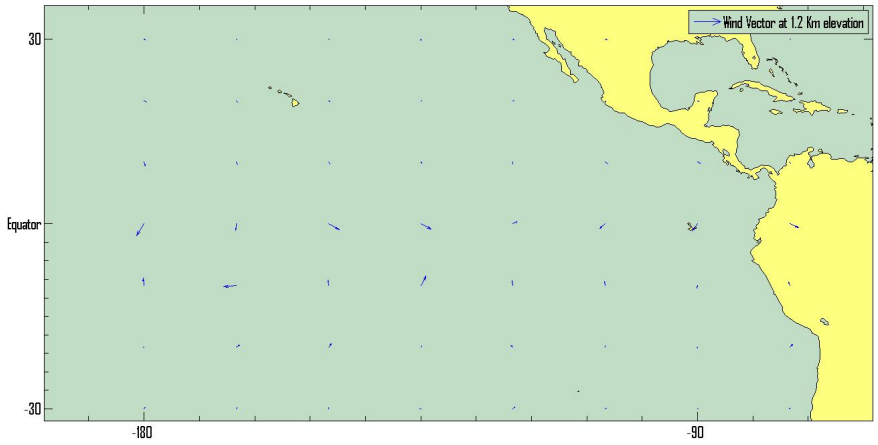

Figure 16: Developed geostrophic field in zones at night times.

E. Future Work

The next step is to characterize the convective heat transfer coefficient "h" in the planetary boundary layer and update the surface energy balance to account for sensible heat flux in the top boundary condition. This allows better finding of the surface temperature which drives the atmosphere dynamics.

Afterwards, the only missing term in the surface energy balance so far is the latent heat which plays a big physical role in oceans as well as wet surfaces. Hence, development of general circulation model based on ocean surfaces will complement what have been done so far for dry land surfaces.

Knowing the earth mask facilitates merging the two models where a careful look must be considered at the interfaces where lateral conduction beneath the surface could not be neglected anymore.

CHAPTER II

WEATHER FORECAST AUTOMATION "ARPS-ADVANCED REGIONAL PREDICTION SYSTEM"

A. Introduction

1. General Introduction

Investigating the main features of large-scale **Synoptic** patterns over the *Eastern Mediterranean* (EM) where Lebanon lies as shown in figure 17 is a key momentous physics in understanding the **Mesoscale** dynamics of the atmosphere. Thus, investigation of the large-scale synoptic patterns over Eurasia for typical *wet* and *dry* months in the EM is useful for understanding the mechanisms responsible for the differences in cyclone orientation and frequencies. Mesoscale meteorology deals with atmospheric dynamics of air that lies in length scales of the the order of 10's km where it is influenced by thermal winds and topography i.e. steep terrains and coasts-seas interface.

Figure 17: Top view for the Eastern Mediterranean "EM" (123tamilchat.com).

It is found that there are unique sea level pressure (SLP) and geopotential height of the 500hpa surface (H-500) anomaly patterns[1] for dry, normal and wet **cool** seasons over the EM and adjacent regions as Europe [4]. Large-scale positive SLP/H-500 anomaly patterns dominate over eastern Europe during the *dry* spells i.e. Some of the established synoptic patterns during dry spells for March case is shown below in figure 18.

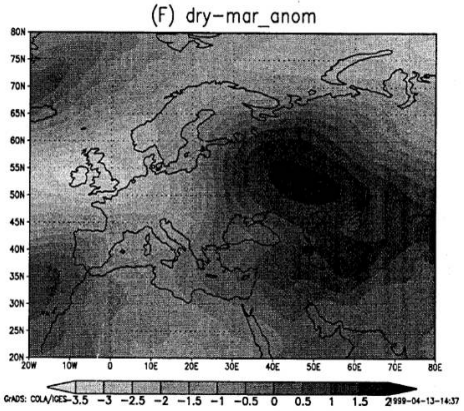

Figure 18: Large-scale SLP anomaly patterns during dry spells over the EM.

While during these periods negative SLP anomaly prevails over southwestern and western Europe. It's the other way around during *wet* cool seasons where negative SLP/H-500 anomaly areas dominate over eastern Europe to north east of the EM and positive SLP/H-500 anomaly patterns occupy western Europe [4]. This is depicted below in figure 19 for March case too.

A trough zone between the Siberian and the Azorean Highs (anticyclones) is positioned over the EM during *wet* spells; however during *dry* spells the Siberian anticyclone is more persistent and thus the center of low surface pressure is now displaced by an offset from the EM to the central part of the northern Mediterranean [4]. This is illustrated below in figure 20.

Analysis of the cyclone tracks in the Mediterranean area made by Alpert et al. (1990a,b) shows that in normal and wet years the region is characterized by higher

[1] Anomaly patterns mean current patterns minus normal patterns.

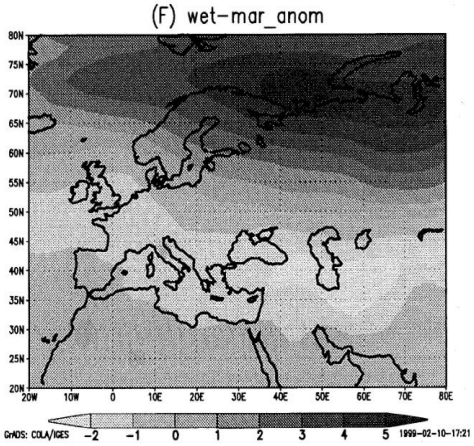

Figure 19: Large-scale SLP anomaly patterns during wet spells over the EM.

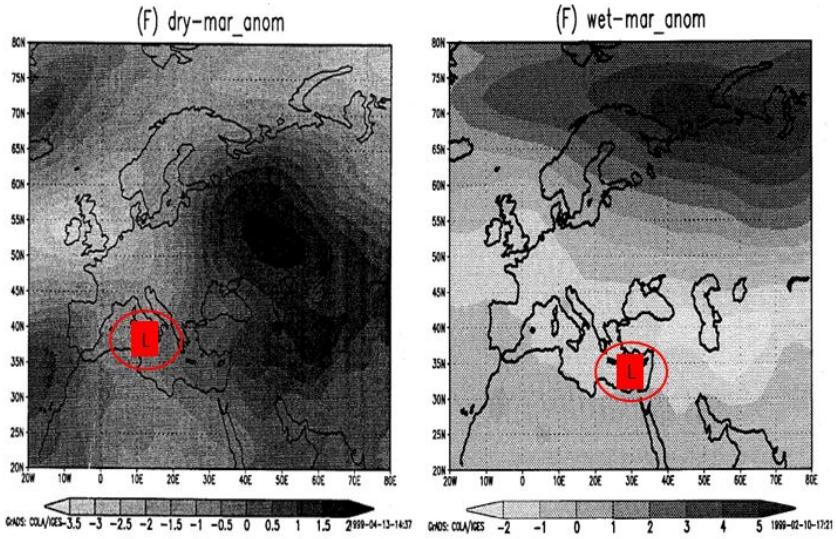

Figure 20: Center of low surface pressure during dry and wet spells over the EM.

frequencies of cyclone tracks [1].

2. Motivation

The aim is to study and assess how well Numerical Weather Prediction Tools (**NWP**) i.e. -**ARPS** software model- can forecast weather for real case scenarios in

Lebanon where a comparison of the prognostic meteorological data is conducted between ARPS simulations and observed measured data. In addition to that, idealized calm situations will be simulated to understand thermal circulations modified by the unique geographic terrain under weak synoptic forcings.

Setting up a weather forecasting tool for Lebanon hosted by the *Mechanical Engineering Department* at the American University of Beirut is the main objective. This setup is to undergo so much tuning (*Sensitivity Study* and *Validation Analysis*).

B. Methodology

1. Numerical Weather Prediction Tools (NWP)

a. ARPS Description

ARPS -Advanced Regional Prediction System- is a numerical model, data assimilation and data processing system, which is envisioned as a prototype for (micro to regional to storm) scale operational prediction which is developed by the Center for Analysis and Prediction of Storms (CAPS) at the university of Oklahoma in 1989, and all associated computer code and documentation are copyrighted to CAPS [9]. ARPS includes a data ingest, quality control, and objective analysis package known as ADAS (ARPS Data Analysis System), assimilation system (ARPSDAS of which ADAS is a component), the numerical prediction model (ARPS Numerical Model), and post processing data (Product Generation and Data Support System) known as ARPSPLT. The numerical forecast component of the ARPS is a three dimensional, nonhydrostatic compressible model solver of the Navier-Stokes equations in generalized terrain-following coordinates which could be run on single processor or massively parallel processors [9]. The main goal attained in ARPS is a developed model system that can be employed in atmospheric research studies and multiscale operational weather prediction.

Development of techniques for the numerical prediction of small-scale weather is attained also in ARPS, with a principal emphasis on increasing substantially the accuracy and reliability of warnings of hazardous events associated with thunderstorms on time scales of one to several hours over spatial domains of several hundred to a few thousand kilometers on a side [9]. The first major development attained in this software is placing about 175 scanning Doppler radars around the US providing approximately continuous coverage of spatial and temporal scales related to storm prediction, and the second major development was finding techniques for retrieving unobserved quantities from radars to model a new consistent set of mass and wind fields appropriate to feed and initialize a storm scale prediction model [9].

b. ARPS Databases

ARPS is linked to databases that provide the software with surface information as described below:

1. Global terrain database with 30-second terrain resolution for most of the US and one degree terrain coverage for the world.
2. Surface energy and moisture budgets with USDA surface characteristics data and associated pre-processing software.

2. Running Up a Simulation

The following criteria is followed to run up a simulation either using "ARPS":

Grid Number	Grid spacing in x-direction dx (m)	Grid spacing in y-direction dy (m)	Grid spacing in z-direction dz_{min} (m)
Grid 1	27000	27000	100
Grid 2	9000	9000	50
Grid 3	3000	3000	25

Table 3: Grid nesting different parameters.

Grid Number	Number of grid points in x-direction nx	Number of grid points in y-direction ny	Number of grid points in z-direction nz	Averaged grid spacing in z-direction dz (m)
Grid N	73	73	35	300

Table 4: Grid nesting common parameters.

a. Grid Nesting and Surface Databases

The center of the mother computational domain is chosen to meet the geographical coordinates -$\varphi = 33.8^o$ (Latitude) and $\lambda = 35.51^o$ (Longitude)- of *Beirut*. The grid nesting -low resolution to high resolution- is generated as if grid domains are zoomed in with respect to the center of the lowest resolution grid (Grid 1) as described in table 3. The intention is to reach a final -High Resolution- grid that captures most of the physics surrounding *Beirut* i.e. influence of the mediterranean sea, and terrain effects of the western mountains chain to the east of *Beirut* as depicted in figure 23. It is recommended to nest the grids in a way that the reduction factor of grid spacing lies in this interval $\frac{1}{3} < \%RF < 1$ as this has been found to optimize both model run time and numerical noise generated in the nesting regions.

After setting up the terrain, surface types (soil texture types-Leaf Area Index) are extracted from their corresponding databases that are available as explained earlier.

The following figures show the mother domain (Grid 1) figure 21, the intermediate domain (Grid 2) figure 22, and the final nested domain (Grid 3) figure 23 respectively.

The 3 grids share some common parameters as described in table 4.

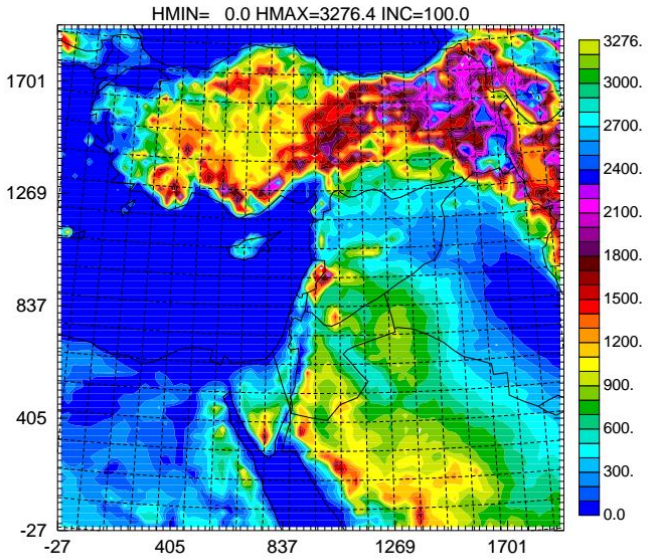

Figure 21: Grid 1: The Mother Lowest Resolution Computational Domain.

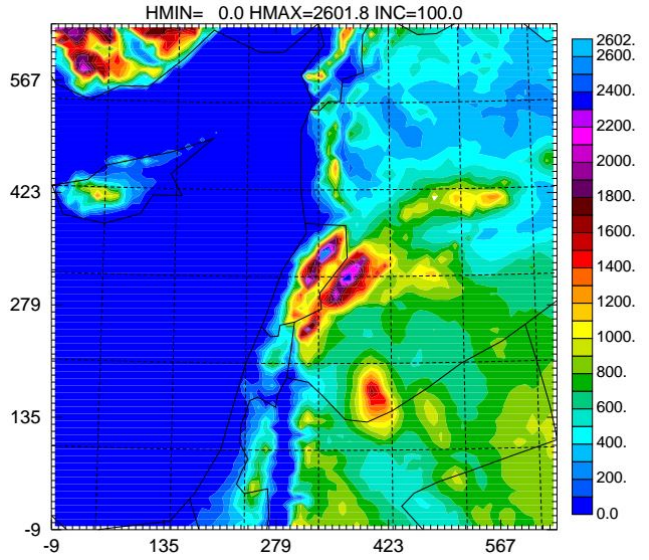

Figure 22: Grid 2: The Intermediate Medium Resolution Computational Domain.

b. Initialization

The synoptic analysis which includes the initial and boundary conditions are extracted from the synoptic scale meteorology datasets currently available that are

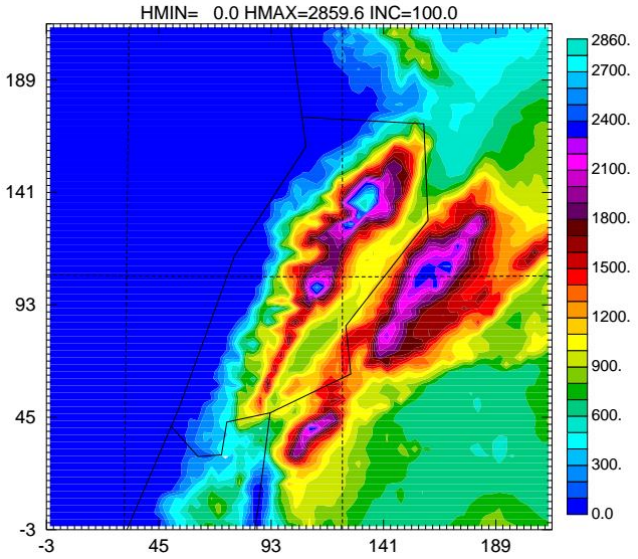

Figure 23: Grid 3: The Final Highest Resolution Computational Domain.

Six-hourly synoptic scale analyses.

The Global Forecast System (GFS) is a weather forecast model produced by the National Centers for Environmental Prediction (NCEP). Dozens of atmospheric and land-soil variables are available through this dataset, from temperatures, winds, and precipitation to soil moisture and atmospheric ozone concentration. The entire globe is covered by the GFS at a base horizontal resolution of 18 miles (28 kilometers) between grid points, which is used by the operational forecasters who predict weather out to 16 days in the future. Horizontal resolution drops to 44 miles (70 kilometers) between grid point for forecasts between one week and two weeks. The GFS model is a coupled model, composed of four separate models (an atmosphere model, an ocean model, a land/soil model, and a sea ice model), which work together to provide an accurate picture of weather conditions.

The synoptic analysis used by the model allows variation of synoptic conditions in three-dimensional space and time, and it feeds the synoptic fields into the model at the boundaries of the outer-most grid -figure 21- every 3 hours.

These forecasts are then used by ARPS mesoscale model to dynamically

downscale the predicitons. The GFS output at 00Z (Zulu Time) -02 EET "Eastern European Time"- and 12Z (14 EET) will be used for ARPS as these are the best 6-hourly representative forecasts that get assimilated initially by atmospheric soundings, so ideally should be better than the rest[2]. These forecasts (00Z and 12Z are posted and available to download for free at 0500Z "0700 EET" and 1700Z "1900 EET" respectively[3].

c. Nudging and Interpolation

After initializing Grid1 (Mother lowest resolution computational domain), the model "ARPS" solves for the prognostic meteorological variables during the specified simulation time period at the nodes of Grid1. Initializing Grid2 is attained after Grid1 simulation ends where *initial and boundary conditions* are interpolated from Grid1 output and to be fed to Grid2. Similarly, Grid3 is initialized when Grid2 simulation ends.

d. Post-processing Output

The available package to plot the prognostic meteorological variables in "ARPS" is ZX-plot (Vector Graphics Package). In the Results section, sample of these images will be shown.

[2]GFS forecast is run every 6 hours and gives predictions at a 3 hour interval for 192 hours (8 days).
[3]The availability for this forecast cycle differs during summer time as follows:

1. Forecast cycle 00Z, posted at 0500Z or 0700 EET (0800 EEST "Eastern European Summer Time").
2. Forecast cycle 12Z, posted at 1700Z or 1900 EET (2000 EEST).

C. Results

1. Real Case Scenario

In the Summer season of 2014 and specifically on June 4^{th}, Lebanon experienced "**Dust Storm over the Mediterranean Sea**". Dust clouds are clearly shown in the short-wave satellite image taken from NASA during that day in figure 24. During that day, strong winds blew dust from the Sahara Desert over the Eastern Mediterranean Sea and reached Beirut which caused a weird increase in temperature at that night where it reached temperatures greater than day temperatures. Such strong winds blow the sand into the air and it can remain airborne for a long time, thus dust clouds can travel long distances. Sand storms originating in the Sahara can travel across the Mediterranean Sea and even reach the European continent.

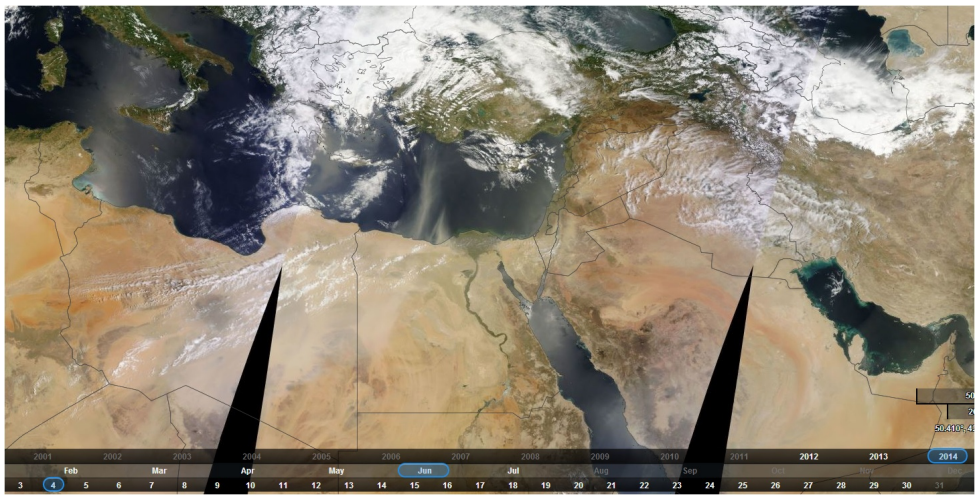

Figure 24: Dust Storm over the Mediterranean.
(https://earthdata.nasa.gov/labs/worldview/)

a. June 2014 Case:

Two major time series plots are generated that include the major meteorological prognostic variables i.e. Wind speed, Wind direction, and Temperature. The latter variables are plotted and compared with available measured data from Beirut airport where the outputs data are extracted from the first grid level of Grid 3 (High Resolution Grid).

The following figure 26 tracks the temperature trend evolution produced by ARPS simulations -black thick line- in the lower part of the figure where the wind direction -black thick line- is superposed too on the upper part of the same figure in order to link and assess the behavior of the temperature profile. The simulation period covers two and a half days starting June, 03, 2014 inclusive.

It is realized that ARPS temperature profile follows smoothly the observed measured temperature profile -red thin line- with an acceptable range offset. For instance, ARPS temperature varies from 25.5 degrees -just before sunrise- to 29.5 degrees -around 12 p.m.- on the second day where the observed (measured) temperature range lies between 23.5 degrees and 30 degrees on that day.

After 12 p.m., the temperature stays increasing steadily even after 6 p.m. influenced by the **Dust Storm**, and this trend is captured in ARPS results where ARPS temperature reaches a maximum of 37 degrees (figure 25) at that night compared to 38 degrees observed measured temperature.

It is noticed that there is a good agreement between observed measured wind direction plot -red thin line- and ARPS wind direction plot -black thick line- where the latter follows to a big extent the observed measured wind direction plot. The wind direction is dominated by *Westerlies* and *South Westerlies* during **days** which implies that the winds are blowing from sea side to land and specifically from North Africa to the Mediterranean, and dominated by *North Easterlies* and by *Easterlies* during **night** which implies that the winds are blowing from land to sea.

Figure 27 tracks the wind speed (Magnitude) trend evolution at an altitude of

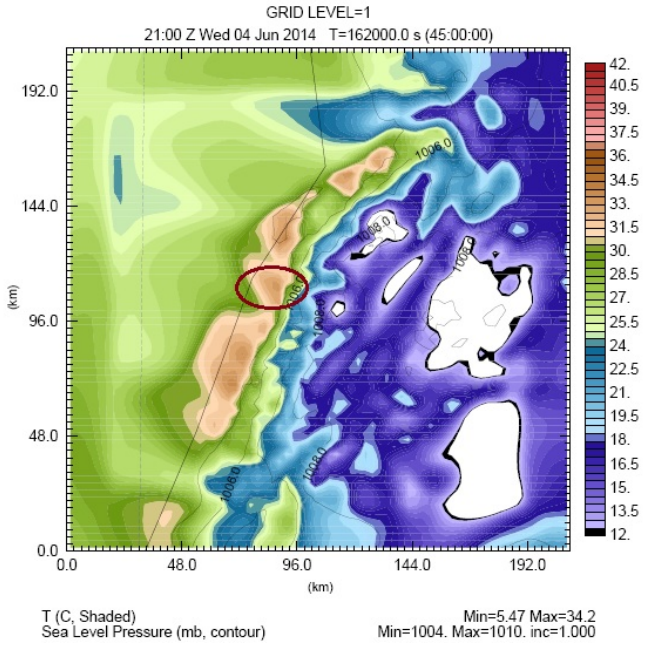

Figure 25: Temperature profile in Lebanon on June 4th, 2014.

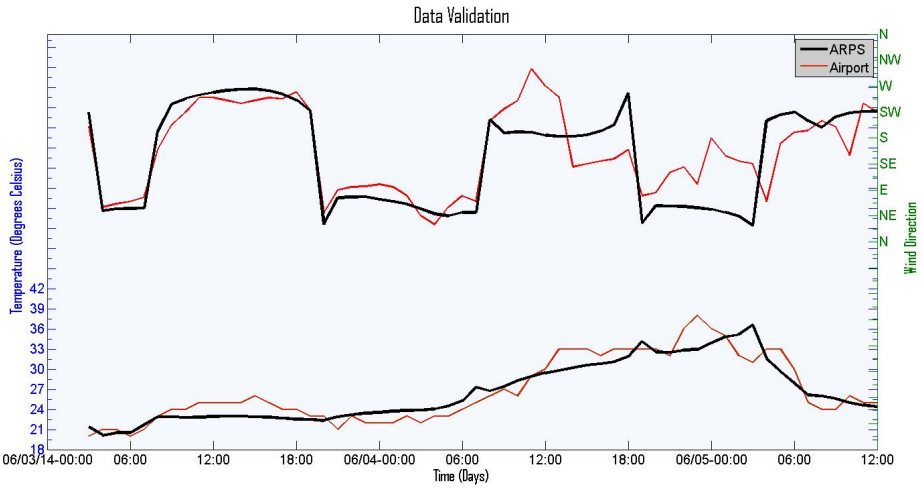

Figure 26: Comparison between ARPS and Observed Temperature Variation vs ARPS and Observed Wind Direction in June 2014.

12.5 m (first grid level of Grid 3) produced by ARPS simulations -black thick line- in the lower part of the figure where the wind direction -black thick line- is superposed too on the upper part of the same figure.

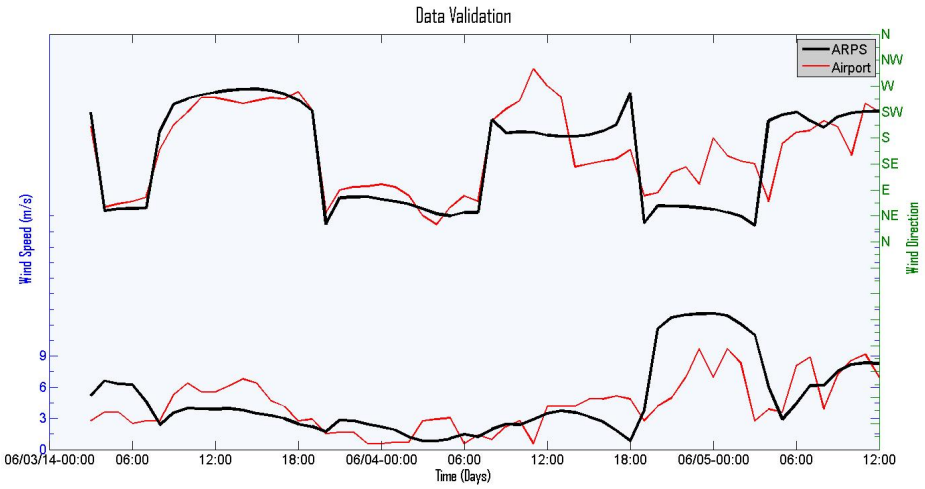

Figure 27: Comparison between ARPS and Observed Wind Speed Variation vs ARPS and Observed Wind Direction in June 2014.

Most of the synoptic scale analysis propagates into the nested grid domains through the boundaries after a day of launching the simulation, and it is realized at this stage that ARPS prediction of wind speed starts to follow the observed measured data i.e on the 4^{th} of June, ARPS's wind speed ranges between almost 1.8 ms^{-1} at midnight to 1.4 ms^{-1} just before sunrise which is expected to be calm as the observed measured data in this interval period. After sunrise, active solar radiation invokes heating of the earth's surface which in turn warms parcels of air in the infinitesimal neighboring layer near the surface. The latter mechanism induces rising motions in the atmosphere because parcels of air are now lighter and less dense. This justifies in general the start of increase in wind speed as predicted by ARPS to reach 3.7 ms^{-1} (peak) at 1:00 p.m. which is near the average measured wind speed at that time. After 6 p.m., wind speed remains increasing influenced by the established **Dust Storm** at that time, where ARPS overpredicted the peak magnitude 11.5 ms^{-1} compared to the measured speed 9 ms^{-1}, and this could be related to the height difference between Beirut airport station and the first grid level of Grid 3.

Looking more into the origin of this storm, the first grid (Grid 1) mother

computational domain is extended to include the Sahara Desert. It is realized that there exists a cyclone in the Mediterranean near North Africa as illustrated in the rectangular box in figure 28 which drives the flow counterclockwise since it's a *Low* in the *northern hemisphere* from the Sahara Desert to the Mediterranean and eventually reaching Lebanon. This justifies the dominance of *South Westerlies* during day times.

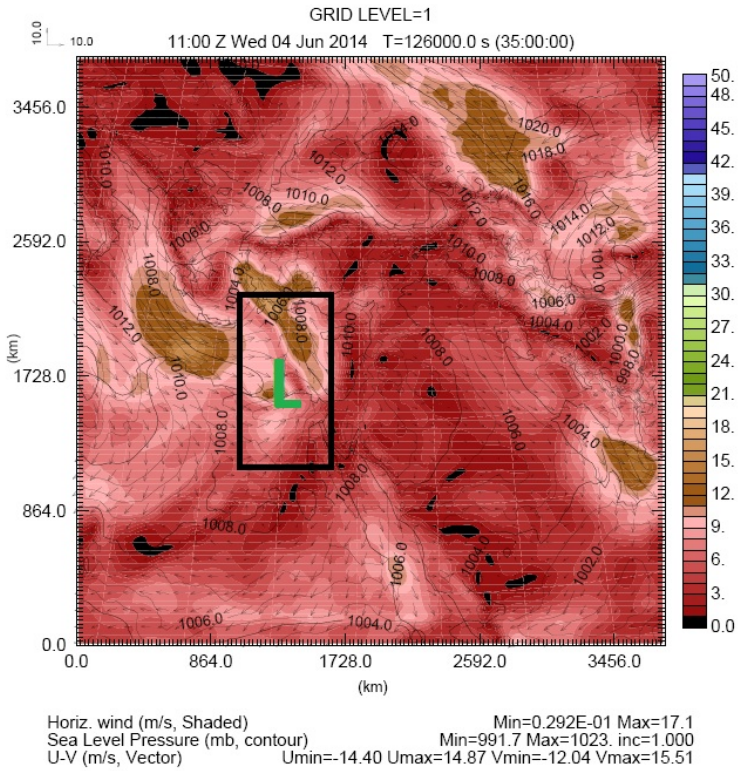

Figure 28: Cyclone over North Africa.

2. Idealized Calm Scenario

Idealized calm situation in Summer is simulated to investigate locally driven thermal circulations which may be modified by the unique geographic terrain under weak synoptic forcings. **July** is chosen as a representative month for Summer.

In order to do so, same methodology is followed as for real case scenarios; however one major modification is made in the synoptic scale forcings. In an idealized calm situation, null initial velocity profile is imposed i.e. everything is at rest. Moreover, dry neutral atmosphere is assumed in our model where potential temperature is non variant in z-direction because the main interest here is to track the evolution of developing local winds when synoptic scales are weak (synoptic winds, temperature and humidity vary with *height* only).

a. Winds Spatial Evolution "Land and See Breezes"

In calm summer situations, during the day the land surface is heated to a higher temperature than the sea. This difference is due in part to the larger heat capacity of the sea, and in part to the consumption of latent heat by evaporation of water. The latter justifies why water surface temperature change reduces to near-zero values during a diurnal cycle. On the other hand, land surface warms and cools more dramatically due to its small molecular conductivity and heat capacity -i.e. soil types- which prevent the diurnal temperature signal from propagating rapidly away from the surface.

Thus, it is expected for the land to be warmer than the sea during the day and cooler at night. Under weak synoptic forcings, this will favor the formation of sea breezes during the day and land breezes during the night along the **coast** where the local meteorology is largely determined by the heterogeneities at the surface and the role of the topography becomes extremely important, even dominant.

As the night deepens, local winds start to form **land breezes** as expected, and

this justifies the presence of *south easterlies* and *easterlies* in the early morning as shown in grid 3 in figure 29.

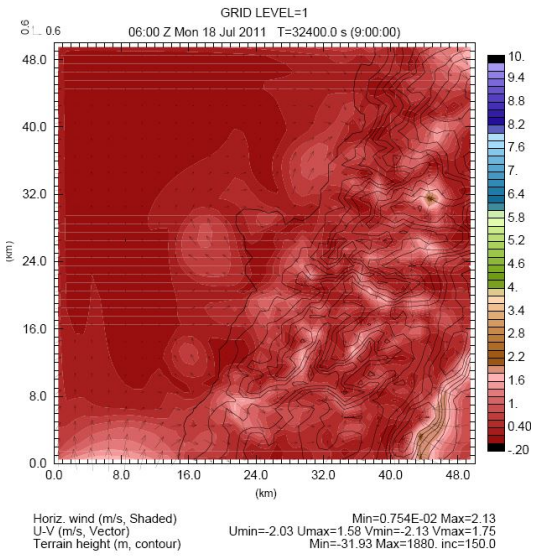

Figure 29: Developed local winds in the early morning in Summer.

As the air parcel acquires speed, the increasing Coriolis acceleration causes it to curve to the right (case of northern hemisphere), and this justifies the presence of *south easterlies*. Cold air from land flows out to sea at low levels, warms, rises, and returns aloft toward land (**anti-land-breeze**) where it eventually descends to close the circulation.

Land breezes continue to evolve during the night and the morning where it starts to decay afterwards due to the different heating rates of land and water (Land starts to warm faster) and formation of **sea breezes** (*north westerlies*) are now favorable as illustrated in figure 30 afternoon (2:00 p.m.) which are influenced by Coriolis force and baroclinicity between land and sea. Cold air from sea flows inwards to land at low levels, warms, rises, and returns aloft toward sea (**anti-sea-breeze**) where it eventually descends to close the circulation.

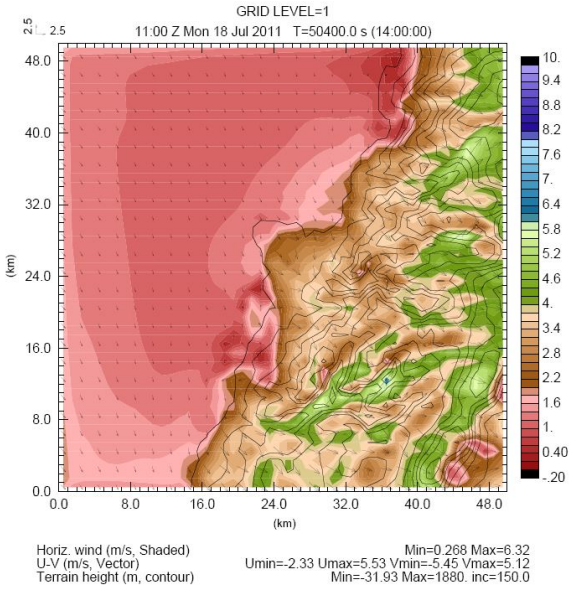

Figure 30: Developed local winds afternoon in Summer.

b. Winds Spatial Evolution "Geographically Generated Local Winds"

It is worth to remember here that the whole analysis is valid under light or calm ambient winds. If it is the other way around, ambient synoptic or mesoscale winds can modify, or even eliminate the weak geographic circulations that will be described below.

During night, nocturnal radiation cools the surface of mountain slopes and consequently cools the air adjacent to it which results in cold downslope known as "**Katabatic Winds**". The chilled air flows into the valley and collects as a cold pool; simultaneously a light return circulation of upward moving air that diverges towards the ridges. This scene will evolve and deepen during the night where continued **Katabatic Winds** feed the cold air pool. Thus, it is expected to realize drainage winds at night flowing *outwards* from high altitudes downslope to low altitudes as depicted in the x-z cross section that crosses Beirut in figure 31 at 2:00 a.m.

During the day, mountains slopes experience warming by sunlight whereas during night nocturnal radiation favors cooling mountain slopes. Such surfaces are warmed or cooled by *conduction* -near the vicinity- and *turbulence*. Air near the

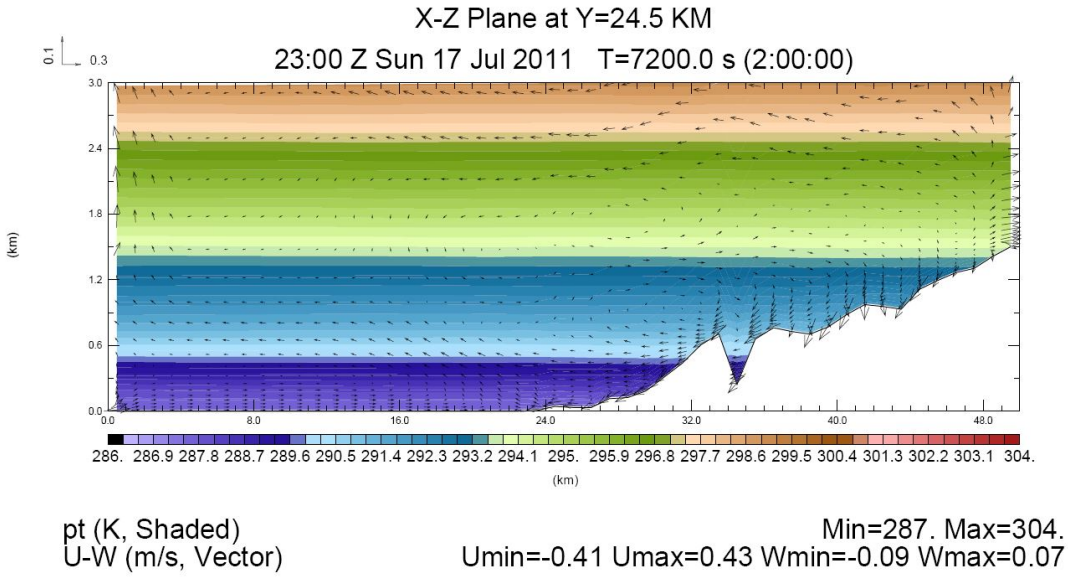

Figure 31: Developed Katabatic Winds at night in Summer.

neighborhood of the surface will then experience different temperature than the ambient air at the same altitude, hence buoyant forces induce a circulation as depicted in the x-z cross section that crosses Beirut in figure 32.

D. Conclusion

At this level and after reaching a working grid simulation for Lebanon. Automation of weather forecast is attained successfully for the first time in Lebanon, and this forecasting tool is to be hosted by the *Mechanical Engineering Department* at the American University of Beirut. This automation is accompanied with neat generated plots for the different prognostic variables. ARPS now is running daily on its own without any external intervention, and all output data for every date are automatically archived.

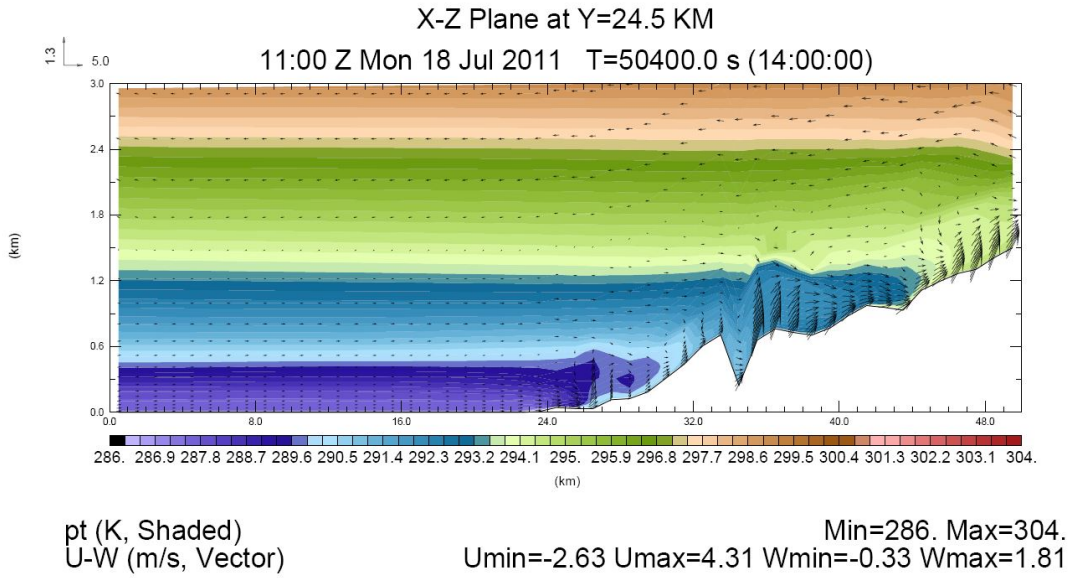

Figure 32: Developed Katabatic Winds during day in Summer.

E. Future Work

In parallel with what have been done, the work to develop a weather forecast website has somehow started to dump the generated images everyday. Website deployment is a vital step at this level.

Applications of multiscale weather and atmospheric modeling may include:

1. Application of the vortex methods to track the planetary boundary layer (PBL) where pollution is trapped.

2. Bekaa Valley: Numerical investigation of the effect of a small terrain feature (i.e. rim) on the mean and turbulent flows inside and downstream of an enclosed basin it surrounds.

3. Weather decision support systems to investigate for instance (i.e. wind turbine siting, precision agriculture -Feasibility study-).

BIBLIOGRAPHY

[1] P Alpert, BU Neeman, and Y Shay-El. Climatological analysis of mediterranean cyclones using ecmwf data. *Tellus A*, 42(1):65–77, 1990.

[2] JW Deardorff. Efficient prediction of ground surface temperature and moisture, with inclusion of a layer of vegetation. *Journal of Geophysical Research: Oceans (1978–2012)*, 83(C4):1889–1903, 1978.

[3] A.E. Gill. *Atmosphere-ocean Dynamics*. Number v. 30 in Atmosphere-ocean Dynamics. Academic Press, 1982.

[4] SO Krichak, M Tsidulko, and P Alpert. Monthly synoptic patterns associated with wet/dry conditions in the eastern mediterranean. *Theoretical and Applied Climatology*, 65(3-4):215–229, 2000.

[5] J. Marshall and R.A. Plumb. *Atmosphere, Ocean and Climate Dynamics: An Introductory Text*. International Geophysics. Elsevier Science, 2007.

[6] T. Muneer. *Solar Radiation and Daylight Models*. Taylor & Francis, 2007.

[7] Suhas Patankar. *Numerical heat transfer and fluid flow*. CRC Press, 1980.

[8] PJ Sellers, RE Dickinson, DA Randall, AK Betts, FG Hall, JA Berry, GJ Collatz, AS Denning, HA Mooney, CA Nobre, et al. Modeling the exchanges of energy,

water, and carbon between continents and the atmosphere. *Science*, 275(5299):502–509, 1997.

[9] Ming Xue, Kelvin K Droegemeier, and Vince Wong. The advanced regional prediction system (arps)–a multi-scale nonhydrostatic atmospheric simulation and prediction model. part i: Model dynamics and verification. *Meteorology and atmospheric physics*, 75(3-4):161–193, 2000.